Magma oscillations in a conduit-reservoir system, application to very long period (VLP) seismicity at basaltic volcanoes–Part II: Data inversion and interpretation at Kīlauea Volcano

Chao Liang[1], Josh Crozier[3], Leif Karlstrom[3], and Eric M. Dunham[1,2]

[1]Department of Geophysics, Stanford University
[2]Institute for Computational and Mathematical Engineering, Stanford University
[3]Department of Earth Sciences, University of Oregon

Key Points:

- Inversions of VLP seismic data favor a short conduit and spherical reservoir over a single crack
- Buoyancy instead of reservoir stiffness is likely to dominate restoring force of VLP oscillations
- Changes in VLP period and decay rate suggest time-varying viscosity and density stratification

Corresponding author: Chao Liang, chao2@stanford.edu

Abstract

Very long period (VLP) seismic events (with dominant periods of 15 to 40 s), observed from 2007 to 2018 at the summit of Kīlauea Volcano, Hawai'i, arise from resonant oscillations in the shallow magma plumbing system. Utilizing an oscillation model developed in the companion paper [*Liang et al.*, 2019], we perform Bayesian inversions on seismic data from four representative VLP events separately for the parameters of the shallow conduit-reservoir system, exploring both sphere and crack reservoir geometries. Both sphere and crack geometries are preferentially located ~1-2 km beneath the northeast edge of Halema'uma'u crater and produce similar fits to the data. Considering a reasonable range for reservoir storativity, magma density, and density contrast between the top and bottom of the conduit, we favor a spherical reservoir with a radius of 0.8 to 1.2 km and a short conduit of less than a few hundred meters. For this geometry, buoyancy from density stratification in the conduit provides the dominant restoring force for the VLP oscillation. Viscosity is constrained within an order of magnitude for each event (e.g., approximately 2 to 23 Pa s for one event versus 27 to 513 Pa s for another). Changes in VLP period T and quality factor Q can be explained by changes in viscosity, density stratification, and/or conduit/reservoir geometry. In particular, observed fluctuations in Q over short time intervals (e.g., hours) with minimal changes in T apparently require rapid changes of magma viscosity by over an order of magnitude, assuming geometry remains unchanged, possibly reflecting changes in volatile content, bubble concentration, or conduit flow regime.

1 Introduction

In active basaltic volcanoes, very long period (VLP, generally considered 2-100 s) oscillations triggered by perturbations in magma pressure offer valuable insights into magma properties and plumbing system geometry [*Rowe et al.*, 2000; *Aster et al.*, 2003; *Mah*, 2003; *Aster et al.*, 2008; *Dawson et al.*, 2010; *Patrick et al.*, 2011; *Chouet and Dawson*, 2011; *Carey et al.*, 2012; *Chouet and Dawson*, 2013; *Orr et al.*, 2013; *Patrick et al.*, 2013; *Dawson and Chouet*, 2014]. Frequently occurring VLP events recorded by broadband seismic stations provide more opportunities for observation than rare explosive events, and are particularly useful in understanding the dynamic evolution of the magmatic system. This study is the second of the two-part companion series. The first part [*Liang et al.*, 2019], hereinafter referred to as Part I, investigates various resonance modes of magma in a coupled conduit-reservoir system. One mode that we term the conduit-reservoir mode has many features in common with the largest amplitude and most common VLP events at Kīlauea Volcano. In Part I we derive a reduced oscillation model for this mode, which we apply in the current study to interpret the VLP seismic signals at Kīlauea Volcano.

VLP seismicity has been recorded at the summit region of Kīlauea Volcano, Hawai'i, since the installation of broadband seismeters in 1994 [*Chouet and Dawson*, 1997; *Ohminato et al.*, 1998; *Almendros et al.*, 2002; *Dawson et al.*, 2004; *Orr et al.*, 2013; *Patrick et al.*, 2011, 2013; *Dawson and Chouet*, 2014]. Since the middle of 2007, highly oscillatory VLP events started to occur and became more frequent after the Overlook crater and associated lava lake were formed on March 19, 2008 [*Wilson et al.*, 2008; *Patrick et al.*, 2011, 2013; *Orr et al.*, 2013; *Dawson and Chouet*, 2014]. These oscillations have distinct onsets, clearly stand out above the background noise, have dominant periods ranging from 15 to 40 s, and last for as long as 10 to 20 minutes. Figure 1 shows a representative VLP event. The current study focuses on the longest period mode that dominates surface displacements (i.e., the conduit-reservoir mode), although shorter period (2 to 20 s) oscillations are also observed in the seismic data [e.g., *Chouet and Dawson*, 2011; *Dawson and Chouet*, 2014]. The temporal alignment (i.e., lack of phase shift) and similarity of waveform shapes at all stations indicate that the solid Earth response is effectively quasi-static for the dominant VLP period, as is expected for these periods given the source-station separation distances (~3 km or less) in the summit broadband network.

The oscillatory VLPs are thought to be triggered by multiple mechanisms, including the final expansion and bursting of rising gas slugs [*Chouet et al.*, 2010], pressure changes induced by rock falls onto the lava lake surface [*Patrick et al.*, 2011; *Carey et al.*, 2012, 2013; *Orr et al.*, 2013], and perturbations at depth that occur without visual manifestation on the lava lake surface [*Dawson and Chouet*, 2014]. Highly impulsive triggers with duration less than the VLP period, such as rockfalls or bubble bursts, excite the eigenmodes or free oscillations of the shallow magma plumbing system, such that the observed period and decay rate are independent of the forcing and are instead determined by the geometry and fluid properties of shallow magma plumbing system. Commonly suggested mechanisms of VLP oscillations, in general, include resonance of waves in magma-filled conduits [e.g., *Garces*, 2000; *Karlstrom and Dunham*, 2016], cracks [e.g., *Chouet*, 1986; *Ferrazzini and Aki*, 1987], large equidimensional chambers [*Shima*, 1958], or a coupled

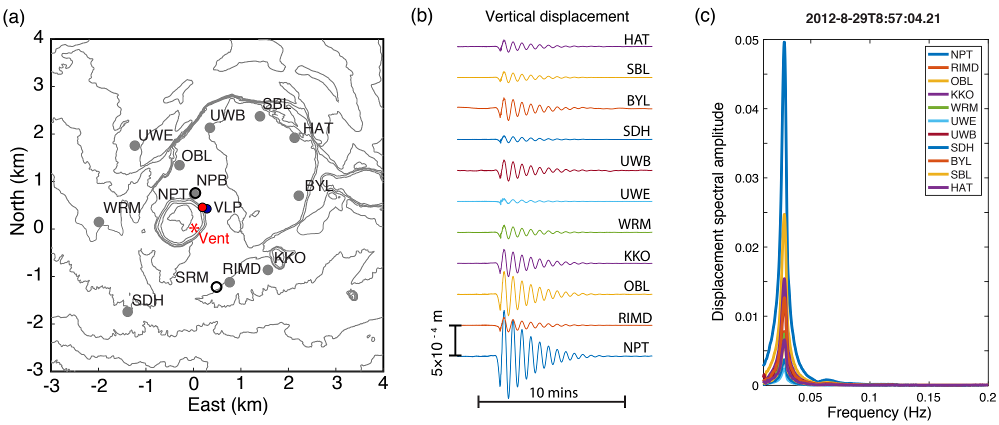

Figure 1. (a) Map of Kīlauea summit caldera showing locations of the broadband stations used in this study. Circles filled with gray are the current network. Stations NPB and SRM (unfilled circles) were replaced by NPT and RIMD, respectively, in June 2011. The red asterisk marks the location of the vent in Halema‘uma‘u crater. The red and blue dots labeled VLP indicate the epicenters of the VLP source by *Chouet et al.* [2010] and *Chouet and Dawson* [2013]. (b) Vertical displacement waveforms of a VLP event at UTC 8:57:04 am, August 29, 2012, after removing the instrument response. (c) Spectral amplitude of the displacement waveforms shown in (b). Note the sharp spectral peaks around 0.0275 Hz.

system of multiple components [e.g., *Chouet and Dawson*, 2013]. However, resonances of acoustic waves in the conduit [e.g., *Garces*, 2000; *Karlstrom and Dunham*, 2016] are not viable mechanisms for the ~30 s oscillations at Kīlauea (see appendix). In particular for Kīlauea, *Chouet and Dawson* [2013] proposed a lumped parameter model to capture the VLP oscillation triggered by rock falls and estimated the conduit geometry and fluid viscosity. In Part I, we showed that this model corresponds to the conduit-reservoir mode, and we extended this model to account for buoyancy and viscous boundary layers in the conduit to provide a more rigorously justified model for forward and inverse modeling.

Central to the conduit-reservoir mode is a shallow magmatic reservoir connected through a conduit to the surface. Point source inversions of seismic data in the 10-50 s band consistently locate a shallow reservoir around 1 km beneath the northeast edge of the Halema‘uma‘u Crater, where pressure changes couple to the solid Earth to generate observable signals on Earth's surface [e.g., *Ohminato et al.*, 1998; *Almendros et al.*, 2002; *Chouet et al.*, 2010]. The VLP source has been interpreted as a dual-dike system [*Chouet et al.*, 2010; *Chouet and Dawson*, 2011, 2013], one trending to the east (2.9×2.9 km) and the other to north (0.7×0.7 km to 2.6×2.6 km), considering fluid dynamic arguments and additional waveform inversions in 1-10 s band. On the other hand, a spherical reservoir at 1-2 km depth beneath the eastern edge of Halemaʻumaʻu Crater is able to explain the geodetically measured surface deformation from longer timescale deflation-inflation (DI) events [*Cervelli and Miklius*, 2003; *Anderson et al.*, 2015]. A recent work (Liang C. and Dunham E.M., 2019. Lava lake sloshing modes during the 2018 Kilauea Volcano eruption probe magma reservoir storativity. Manuscript submitted to Earth and Planetary Science Letters, referred to hereafter as Liang and Dunham 2019), using the very long period lava lake sloshing modes (10-20 s) during the 2018 Kīlauea eruption, show that the reservoir storativity (volume change per unit pressure change) during the 10-20 s oscillations is bounded to be higher than 0.4 m^3/Pa, consistent with the estimates (0.21-0.46 m^3/Pa) from the DI events by *Anderson et al.* [2015]. Therefore, it is highly likely that the ~30 s VLP oscillations activate the same reservoir as the DI events and thus share similar reservoir storativity.

In this work, we estimate the geometry and fluid properties of a coupled conduit-reservoir system by joint inversions of the surface displacement patterns, oscillation periods, and decay rates of VLP oscillations in a Bayesian framework. We assume that the shallow magma plumbing system is represented by a cylindrical conduit extending from the bottom of the lava lake to a reservoir and test two reservoir shapes: a tabular square-shaped crack and a sphere. An examination of the dual-dike reservoir system proposed by *Chouet and Dawson* [2011, 2013] is beyond the scope of the current study. We model the periods and decay rates of the VLP oscillations with the reduced conduit-reservoir model developed in Part I, capturing the dominant balance between inertia of magma oscillating in conduit and restoring forces from buoyancy and reservoir stiffness. We invert the seismic data of four representative VLP events for the conduit and reservoir properties using the Markov Chain Monte Carlo (MCMC) method, quantifying estimation uncertainty. The reservoir storativity, defined as the volume change of magma in the reservoir per unit pressure change, is required to be consistent with the inverted reservoir geometry. We identify parameter combinations that can be constrained from the data and discuss the trade-offs among different parameters. Finally, we discuss limitations of VLP seismic data in constraining the properties of the plumbing system and suggest possible observations that might reduce certain ambiguities left unresolved in our study.

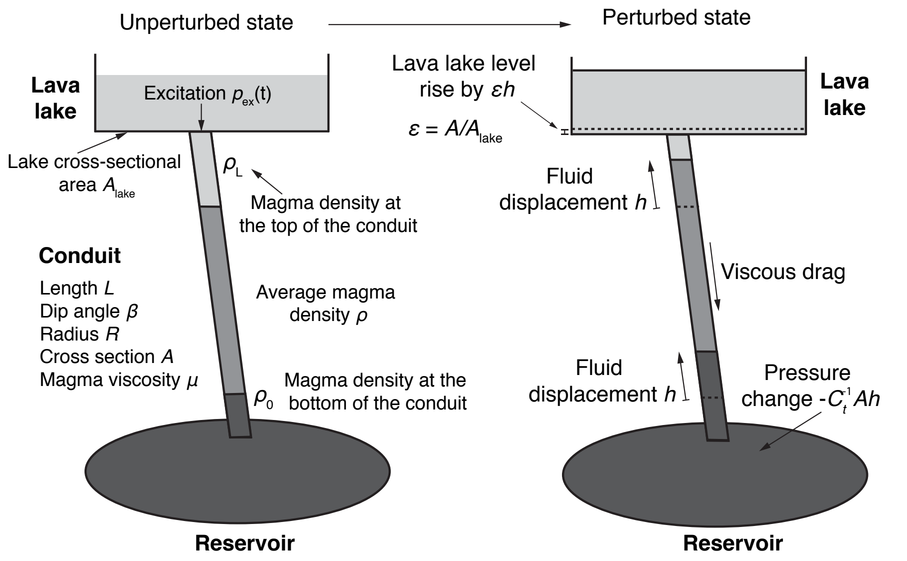

Figure 2. Schematic of the conduit-reservoir system. The conduit, filled with incompressible and viscous magma, is cylindrical with constant radius and connects the lava lake to the reservoir. The system is perturbed by external forcing pressure $p_{ex}(t)$ at the top of the conduit. Fluid displacement in the conduit induces changes in the weight of fluid in the conduit due to the density contrast $(\rho_0 - \rho_L)$ between the bottom and top of the conduit, hydrostatic pressure change at the bottom of the lava lake due to fluctuation of lava lake level, change in reservoir pressure from the reservoir stiffness, and viscous drag along the conduit. The colors in the schematics are for illustration purposes and do not imply any particular density profile.

2 Forward model

2.1 Oscillation model

We model the VLP oscillation using the conduit-reservoir model developed in Part I, considering fluid inertia, buoyancy, and viscosity in the conduit, and reservoir storativity, while neglecting fluid inertia and viscous dissipation in the reservoir and fluid compressibility in the conduit. This model is an extension of the lumped parameter model proposed by *Chouet and Dawson* [2013] by including gravity (buoyancy) and a rigorous treatment of viscous boundary layers along the conduit walls. We refer the readers to Part I for a detailed derivation of the oscillation model and justification of model assumptions. Here, we briefly summarize key governing equations for this paper to be self-contained.

Consider a rigid cylindrical conduit of length L and radius R connected to a reservoir at the bottom and to a lava lake (with cross-sectional area A_{lake}) at the top, as shown in Figure 2. Magma in the conduit has density ρ_0 at the bottom, ρ_L at the top, ρ on average, and a constant viscosity μ. The system is set into oscillation by an impulsive external excitation $p_{ex}(t)$ at the top of the conduit, which is the pressure change induced by a complex set of reaction forces inside the lava lake such as the rock fall impact, bubble bursting, and viscous drag as the rock sinks in the lake. The equations governing motion of magma in the conduit are

$$\rho L \frac{\partial v}{\partial t} = -\Delta\rho g h \sin\beta - C_t^{-1} A h - \mu L \frac{1}{r}\frac{\partial}{\partial r}\left(r\frac{\partial v}{\partial r}\right) - p_{ex}(t), \quad (1)$$

$$\frac{dh}{dt} = u, \quad (2)$$

$$u = \frac{1}{A}\int_0^R v 2\pi r dr, \quad (3)$$

where $v = v(r,t)$ is magma velocity along the conduit (positive vertical up) with $v(R,t) = 0$ (no slip condition at the conduit walls), $u = u(t)$ is cross-sectionally averaged velocity, $h = h(t)$ is magma displacement, $A = \pi R^2$ is conduit cross-sectional area, g is gravitational acceleration, and β is the dip angle of the conduit ($\beta = \pi/2$ is vertical). In addition, $\Delta\rho = (\rho_0 - \rho_L) + \epsilon \sin(\beta)^{-1}\rho_L$, $\epsilon = A/A_{lake}$, and C_t is the total reservoir storativity. The storativity quantifies the injected magma volume, $-Ah$, required to produce unit reservoir pressure change, p_r. At Kīlauea, given a lava lake of dimension ~160 × 200 m [*Chouet and Dawson*, 2013] and a sub-vertical conduit of radius ~5 m [*Fee et al.*, 2010; *Chouet and Dawson*, 2013], $\epsilon \approx 0.0007 \ll 1$. Therefore, we assume $\epsilon = 0$ so $\Delta\rho = \rho_0 - \rho_L$.

As shown in Part I, the total reservoir storativity C_t depends on both the magma compressibility β_m and elastic compliance of the reservoir or chamber β_c as $C_t = (\beta_m + \beta_c)V$, where V is the reservoir volume [e.g., *Rivalta and Segall*, 2008]. However, since C_t is the only parameter that describes the reservoir in the oscillation model, the relative contributions of β_m and β_c cannot be discriminated. In this work, we neglect magma compressibility. This assumption is well justified for a crack but not necessarily for a sphere (see Part I). In the case of a spherical reservoir, neglecting magma compressibility in our inversion will result in an overestimate of reservoir compliance. Therefore, the reported size of a spherical chamber in this study should be viewed as an upper bound estimate. For a sphere with radius a embedded in a solid with shear modulus G and Poisson ratio ν_s, $C_t = 8a^3/(3G^*)$ [*Mogi*, 1958] where $G^* = G/(1-\nu_s)$. For a tabular crack with length D and aspect ratio of order unity, a similar scaling relation exists: $C_t \sim D^3/G^*$, although the nondimensional prefactor must be calculated numerically using, for example, the displacement discontinuity method (DDM) for dislocations in an elastic half-space

[*Crouch et al.*, 1983; *Okada*, 1985, 1992] as we have done in Part I. For simplicity, we assume a square crack in this study. The total storativity C_t is independent of crack width w_0, so the current method can not be used to determine w_0. We assume $G = 10$ GPa and $\nu_s = 0.25$, consistent with the average values of the Kīlauea summit 3-D structure by *Dawson et al.* [1999] and typical for shear moduli (1-30 GPa) in volcanic areas [e.g., *Ryan*, 1987; *Rivalta and Segall*, 2008]. Although not modeled in this study, uncertainty in G adds additional uncertainty in estimated reservoir geometry. For instance, if G is increased by a factor of 3 to 30 GPa, then the estimated sphere radius or crack length will increase by a factor of $3^{1/3} \approx 1.4$.

As shown in (1), during the oscillation, fluid inertia in the conduit is balanced by buoyancy ($-\Delta\rho g h \sin\beta$), reservoir stiffness ($-C_t^{-1} A h$), viscous drag, and external forcing. Without viscosity, $v = u$, so that (1), in the absence of external forcing, is

$$\rho L \frac{\partial^2 h}{\partial t^2} = -\left(\Delta\rho g \sin\beta + A C_t^{-1}\right) h, \tag{4}$$

which is an undamped harmonic oscillator with natural period

$$T_0 = 2\pi \sqrt{\frac{L\rho}{\Delta\rho g \sin\beta + A C_t^{-1}}}. \tag{5}$$

The relative importance of the two restoring forces (buoyancy and reservoir stiffness) is quantified by the dimensionless stiffness ratio

$$\lambda = \frac{A}{C_t \Delta\rho g \sin\beta}. \tag{6}$$

When $\lambda \gg 1$ (the stiff reservoir limit), reservoir stiffness dominates over buoyancy, and vice versa for $\lambda \ll 1$ (the buoyancy-dominated limit). For a viscous magma ($\mu > 0$), the natural period T of the damped system is longer than T_0 and the decay rate is quantified by a finite quality factor Q, defined as the number of oscillations required for a free oscillating system's energy to fall off to $e^{-2\pi}$ or about 0.2% of its original energy [*Green*, 1955]. As shown in Part I, the ratio $T^* = T/T_0$ and quality factor Q are determined by the single dimensionless parameter

$$\chi = \frac{T_0/2\pi}{\tau_{vis}}, \tag{7}$$

which can be regarded as the ratio between the undamped oscillation period T_0 and the momentum diffusion time across the conduit radius,

$$\tau_{vis} = R^2/\nu, \tag{8}$$

where $\nu = \mu/\rho$ is the kinematic viscosity. As shown in Part I, T_0 does not differ much from T unless Q is small (less than 5), so except in this special case T is a good indicator of T_0 while Q is directly linked to τ_{vis}. More discussion of the physical interpretation of χ and its quantitative relations with T^* and Q are given in Part I.

2.2 Surface displacement

The observable surface displacements are caused by pressure changes within the reservoir. Displacements contributed by pressure and shear traction changes in the conduit are negligible in comparison. Because the response of both the conduit-reservoir system and solid are effectively linear, the surface displacement spectrum $\hat{\mathbf{u}}(\omega)$ is proportional to the spectrum $P_{ex}(\omega)$ of the external excitation $p_{ex}(t)$, where ω is angular frequency. As shown in Part I, the transfer function between $P_{ex}(\omega)$ and $\hat{\mathbf{u}}(\omega)$ scales as the product of $AT_0^2/(\rho L)$ and another function that can be calculated given the reservoir location, reservoir shape, relative magma and reservoir compressibilities, the elastic properties of the solid, and parameter χ. The system's response is amplified near the resonant frequency $\omega_r = 2\pi/T$ but remains finite due to the presence of viscosity.

While any $p_{ex}(t)$ can be used in our model, in this study we assume an impulsive excitation in which $p_{ex}(t)$ is nonzero only over a duration much shorter than the VLP period, such that

$$p_{ex}(t) \approx P_{ex}\delta(t - t_c), \tag{9}$$

where t_c is the center time of the impulse and P_{ex} is the amplitude (and frequency-independent spectrum) of the impulse. Solving (1)-(3) in the frequency domain, we obtain the reservoir pressure change at the resonant frequency ω_r, which is then related to surface displacements through quasi-static elasticity. The quasi-static elasticity assumption is appropriate given the long time scale and relatively short source-station distances at the Kīlauea summit network. The quasi-static assumption is also justified by the observation of minimal wave propagation effects (e.g., phase differences) in the VLP data (see appendix). For a spherical reservoir, we include the finite source corrections in *McTigue* [1987]. For a tabular crack, we discretize the crack into an 8×8 grid of square elements and calculate the opening for each element under uniform pressure [e.g., *Segall*, 2010]. We then sum the displacement contributions of all elements [*Okada*, 1985]. Topography is neglected and the surface of the elastic half-space is set at the height of the instruments.

We account for the additional contribution of tilt to the surface displacement recorded by seismometers, which can be substantial in horizontal displacements at very long periods [*Maeda et al.*, 2011; *Chouet and Dawson*, 2013]. The predicted displacement spectrum at $\omega = \omega_r$ is

$$\hat{\mathbf{u}} = \left[\mathbf{G}^{trans} + \mathbf{G}^{tilt} \frac{g}{(i\omega_r)^2} \right] P_{ex}, \tag{10}$$

where $\mathbf{G}^{trans}$ and $\mathbf{G}^{tilt}$ are the Green's functions for ground translation and tilt given unit external excitation at the top of the conduit.

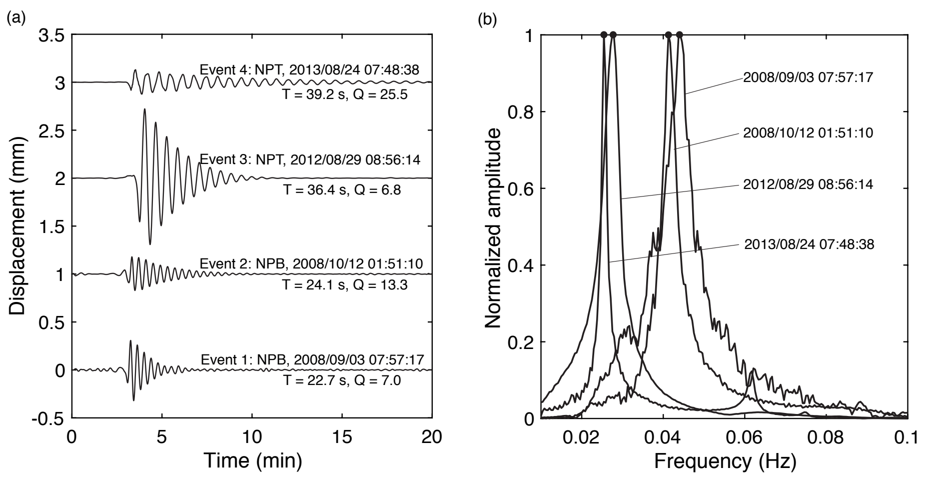

Figure 3. (a) Vertical displacement waveforms (after removing instrument response) and (b) normalized spectral amplitudes at NPT/NPB station for four selected VLP events. The two events in 2008 are band-pass filtered to 10-50 s and two events after 2011 are filtered to 10-100 s. The signal start times (UTC), dominant periods, and quality factors are indicated in the labels. The black dots in (b) mark the modeled VLP modes.

3 Data

The broadband seismic network at the summit of Kīlauea at the time of the studied VLP events features 11 three-component stations covering an aperture of ~5 km [*Chouet and Dawson*, 2013], as shown in Figure 1a. Station UWE was added to the network in 2010 and stations NPB and SRM were replaced by NPT and RIMD in June 2011 [*Chouet et al.*, 2010]. In this study, we select four representative VLP events over multiple years with various periods and decay rates from the catalog compiled by *Dawson and Chouet* [2014] for analysis, shown in Figure 3a. Events 1 and 2 in 2008 are associated with vigorous degassing (Type 1) while events 3 and 4 are triggered by rockfalls (Type 2) [*Dawson* *and Chouet*, 2014]. Both event types excite the VLP oscillation in a relatively impulsive manner, as assumed in our model.

To prepare the data for inversion, some processing steps need to be carried out (see appendix) to extract the resonant period T, quality factor Q, and real parts of spectral values of surface displacements $\hat{u}_i^R$ at the resonant period, with i indicating the channel index. Instead of following *Chouet et al.* [2010] and *Chouet and Dawson* [2013], who invert the full spectrum of the seismic data at 10-50 s band, we only invert the system's response at the resonant period T. The spectra $\hat{u}_i^R$, complemented by T and Q, are sufficient to characterize the mode. This approach not only reduces the number of evaluations of the forward model, which improves the computational efficiency, but also excludes the interference from higher resonant modes, such as the 10-20 s lava lake sloshing modes identified by *Dawson and Chouet* [2014], that may have different oscillation mechanisms and surface displacement patterns from the longest period mode.

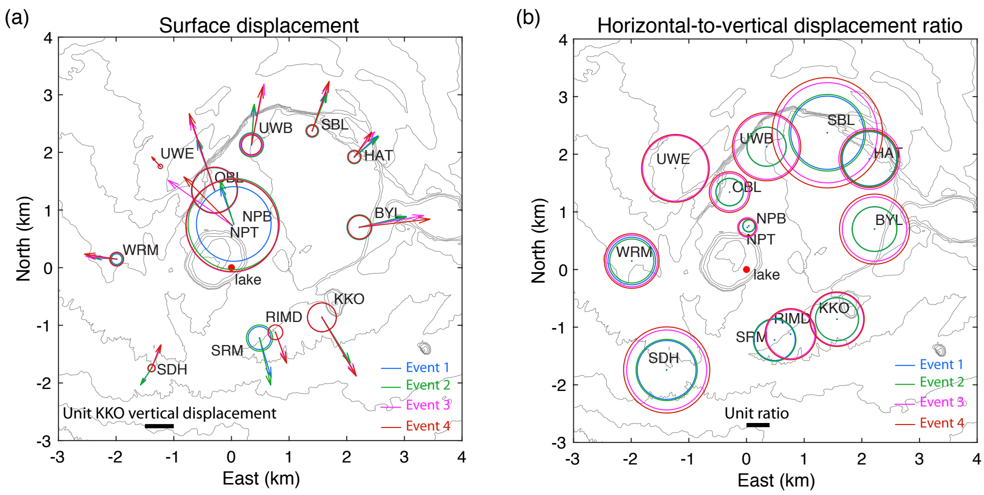

Figure 4. (a) Spatial pattern of normalized surface displacement and (b) horizontal-to-vertical displacement ratio of four selected VLP events calculated using $\hat{u}_i^R$. Diameters of circles in (a) are vertical up displacements and arrows indicate horizontal displacements. Displacements are normalized by the vertical component of KKO. Diameters of circles in (b) indicate horizontal-to-vertical displacement ratios. All events are characterized by vertical uplift/depression and horizontal expansion/contraction and by greater horizontal-to-vertical displacement ratios at stations farther away from the lava lake. Events 3 and 4 have higher horizontal-to-vertical displacement ratio than events 1 and 2.

The surface displacements $\hat{u}_i^R$ are plotted in Figure 4. Note that due to the change in the monitoring network in 2011 stations NPB and SRM only recorded events 1 and 2 and stations UWE, RIMD, and UWE only recorded events 3 and 4. Therefore, we normalize $\hat{u}_i^R$ with the vertical component of KKO, one of stations that recorded all four events. All events are characterized by vertical uplift/depression and horizontal expansion/contraction and by greater horizontal-to-vertical displacement ratios at stations farther away from the center, implying a deformation source that has a significant volumetric component. The vertical displacement patterns of all events are remarkably similar, despite the events having different periods and quality factors. The orientations of the horizontal components are also very similar among all events except that events 3 and 4 have significant westward motion at station NPT. Events 3 and 4 exhibit considerably higher horizontal-to-vertical displacement ratios at nearly all stations compared to events 1 and 2. The inward motion at station SDH for events 3 and 4 seems incompatible with the overall deformation pattern and thus this station is discarded in our inversions.

4 Inversion method

The extracted features (T, Q, and $\hat{u}_i$) are matched by predictions from the forward model by adjusting the model parameters shown in Table 1 using a Bayesian inversion approach that accounts for the data uncertainty. We assume that the conduit directly connects the bottom of the lava lake (at depth Z_0) to the reservoir and do not treat the conduit length L and dip β as independent parameters. For a crack-shaped reservoir, the conduit is connected to the crack centroid. For a spherical reservoir, the conduit is pointed toward the centroid but only reaches the sphere's surface. Therefore, $L = \sqrt{X_c^2 + Y_c^2 + (Z_c - Z_0)^2}$ for a crack and $L = \sqrt{X_c^2 + Y_c^2 + (Z_c - Z_0)^2} - a$ for a sphere. The conduit dip $\beta = \arcsin\left((Z_c - Z_0)/\sqrt{X_c^2 + Y_c^2 + (Z_c - Z_0)^2}\right)$. We require $Z_c > Z_0$ in the inversion, which forces the top of the reservoir to be deeper than the bottom of the lava lake.

In a Bayesian framework, model parameters $\mathbf{m}$ are treated as random variables. According to Bayes' theorem, the posterior probability density function (PDF) of $\mathbf{m}$ conditioned on the data $\mathbf{d}$ is

$$P(\mathbf{m}|\mathbf{d}) \propto P(\mathbf{d}|\mathbf{m})P(\mathbf{m}), \tag{11}$$

where $P(\mathbf{d}|\mathbf{m})$ is the data likelihood function and $P(\mathbf{m})$ is the prior distribution. The prior distribution reflects the information we know about the model parameters before collecting any data. The data likelihood function is a measure of the misfit between the predicted and observed data, and its distribution reflects the data uncertainty due to the presence of noise. After observing the data, our knowledge about the model parameters is updated to $P(\mathbf{m}|\mathbf{d})$ from $P(\mathbf{m})$ because some parameter combinations are unlikely to produce the observed data. We assume uniform prior distributions with specified bounds and a Gaussian likelihood function (see appendix). Finally, posterior PDFs are then sampled using an MCMC approach [e.g., *Mosegaard and Tarantola*, 1995]. We use the software GWMCMC developed by *Grinsted* [2014], which implements the affine invariant ensemble MCMC sampler [*Goodman and Weare*, 2010].

To compare two reservoir geometries (crack and sphere) and test the significance of adding more model parameters, we use the Bayesian Information Criterion (BIC) [*Schwarz et al.*, 1978] defined as

$$\mathrm{BIC} = \ln(N)k - 2\ln(L^*), \tag{12}$$

where N is the number of observations, k is the number of model parameters, and L^* is the maximum value of the likelihood function (C.1). Since we use a uniform prior, the maximum likelihood estimate (MLE) is the same as the maximum a posteriori probability (MAP) estimate. A source model with a lower BIC is preferred, which favors a lower misfit but penalizes the number of model parameters. A BIC difference larger than 10 is considered statistically very strong evidence against the model with a higher BIC [*Kass and Raftery*, 1995]. However, due to numerous assumptions made in the forward model, we also consider the physical interpretability of the MLE solution. We use misfit functions similar to *Chouet and Dawson* [2013] to aid the evaluation of the MLE (see appendix).

5 Results

Here we present results from our inversions. For both the conduit-sphere and conduit-crack models, the best-constrained parameters are the reservoir location and the parameter combinations (T_0 and τ_{vis}) that determine the observable oscillation period T and quality factor Q (Figure 5), as anticipated from the forward model (see Part I). Below we discuss solutions for the conduit-sphere and conduit-crack models separately, highlighting key findings and parameter trade-offs. Some figures contain results for all four VLP events, whereas others exclusively focus on event 4 as a representative example, with similar figures for the other events appearing in the Supporting Information.

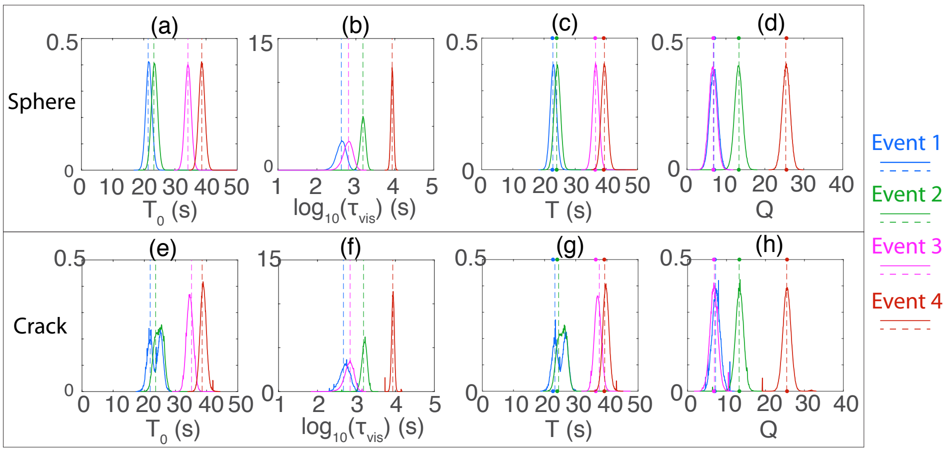

Figure 5. Distributions (solid lines) of T_0, τ_{vis}, T, and Q for the conduit-sphere model (a-d) and conduit-crack model (e-f), calculated from the posterior samples obtained from MCMC inversions. The vertical dashed lines indicate the MLE. In (c-d) and (e-h), the dots indicate the observed T and Q.

5.1 Conduit-sphere model

For the conduit-sphere model, the sphere centroid location is well constrained and consistent over the four studied VLP events, as shown in Figure 6f–h. For example, the sphere centroid for event 4 (Figure 7a) is located at the northeastern edge of the Halema'uma'u crater (0.41 km east and 0.37 km north from the lava lake) and at a depth of about 1.27 km. The centroid locations for events 1 and 2 are close to each other and are about 0.2 km deeper than events 3 and 4.

As seen in Figure 6i, two solutions for sphere radius a exist, one larger (0.8-1.25 km) and the other smaller (0.2-0.4 km) for events 1 and 2. The separation between the two solutions are less distinct for events 3 and 4. The large sphere (a > 0.5 km) solution corresponds to the buoyancy-dominated limit ($\lambda \ll 1$), as seen in Figures 7a and 8b. In the small sphere (a < 0.5 km) solution, λ can be comparable to or even much larger than unity, corresponding to the reservoir stiffness limit (Figures 7a and 9b). Both the small and large sphere solutions fit the data equally well for event 4 as shown in Figure 7a, as is also the case for the other events (see Supporting Information). As shown in Figure 7b, a sphere radius smaller than 0.5 km implies a storativity C_t smaller than ~0.03 m^3/Pa. In contrast, the large sphere solution has a larger storativity that is far more consistent with previous estimates, 0.21-0.46 m^3/Pa, from geodetic analysis of DI events by *Anderson et al.* [2015].

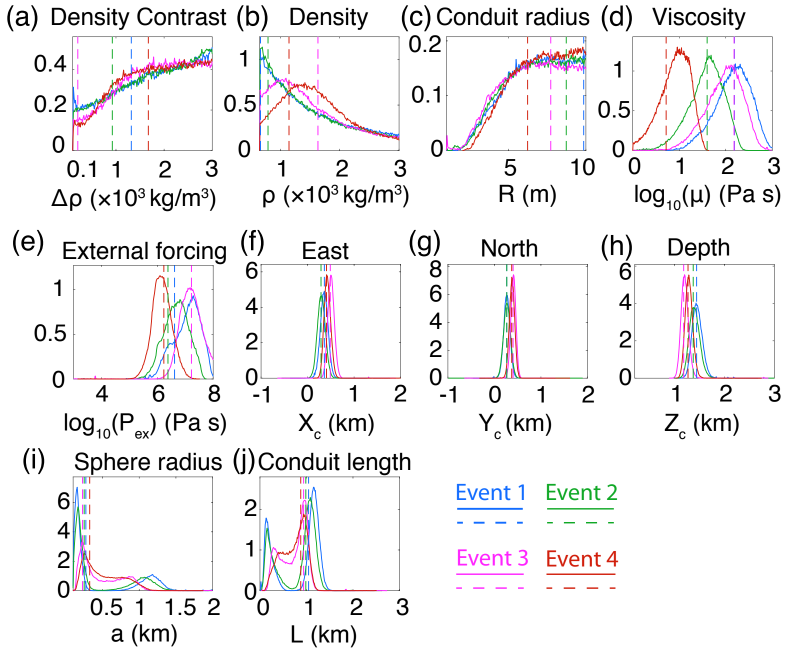

Figure 6. Posterior distributions (solid lines) of model parameters of the conduit-sphere model for four VLP events with 4 million samples. The conduit length L is calculated from the posterior PDFs of the sphere radius and centroid location while all other parameters are directly estimated in the MCMC inversion. The vertical dashed lines indicate the maximum likelihood estimate (MLE).

The observed period and quality factor constrain two parameter combinations (T_0 and τ_{vis}), as shown in Figure 5. The differences in T and Q of the four events intrinsically reflect fluctuations of T_0 and τ_{vis} in the plumbing system. Well constrained T_0 and τ_{vis} are then the basis for understanding the complex trade-offs among other individual parameters, as shown in Figures 8 and 9 for the large and small sphere limits, respectively. Despite some parameter trade-offs, magma viscosity is constrained within an order of magnitude. For events 1 and 4, the MLE viscosities are 154.9 Pa s with 90% credible intervals [27, 513] Pa s and 5.2 Pa s with 90% credible interval of [2.1, 22.9] Pa s, respectively (see Supporting Information). Due to higher Q, lower viscosities are estimated for events 2 and 4 as compared to events 1 and 3.

We now use event 4 as an example to discuss parameter trade-offs in the large and small sphere limits. Similar trade-offs are found for other events (see the Supporting Information). When a is larger than 0.5 km, the restoring force is dominated by buoyancy (λ

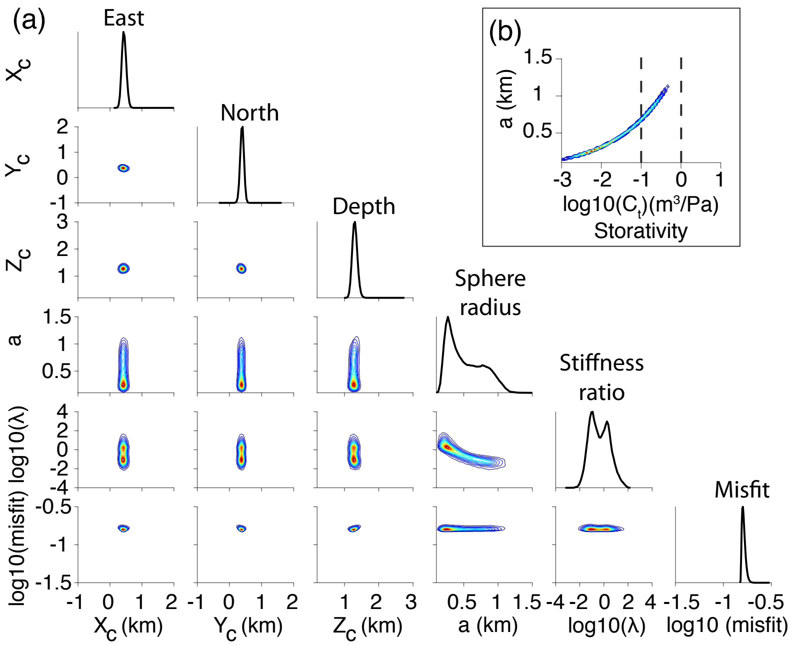

Figure 7. Event 4. (a) Correlation plots of model parameters for the sphere, stiffness ratio λ, and misfit. The large sphere (a > 0.5 km) solutions correspond to the buoyancy limit ($\lambda \ll 1$). (b) Correlation plots between reservoir storativity (C_t) and sphere radius. Two dashed lines mark the range 0.1-1 m^3/Pa.

$\ll$ 1), as shown in Figure 8b, and hence

$$T_0 \approx 2\pi\sqrt{\frac{L\rho}{\Delta\rho g \sin\beta}}. \tag{13}$$

This explains the trade-offs among $\Delta\rho$, ρ, and L that are evident in Figure 8a. To explain the observed period, $\Delta\rho$ is required to approximately scale with ρ and the $\Delta\rho/\rho$ ratio is determined by T_0 and L. A shorter period (as in events 3 and 4, see Supporting Information) or a longer conduit requires higher $\Delta\rho/\rho$. The estimated L ranges from 200 to 700 m, with shorter conduits corresponding to larger spheres. The reduction of conduit length at large a is the key to keep $\Delta\rho/\rho$ within a reasonable range. For event 4, the 90% credible intervals for $\Delta\rho$ and ρ are 740-2900 kg/m^3 and 770-2600 kg/m^3.

Parameter trade-off becomes more complex in the small sphere limit because the restoring force from reservoir stiffness then dominates. The presence of AC_t^{-1} in (5) explains the trade-off between R and a shown in the small sphere results (Figure 9a), which is not observed in the large sphere results (Figure 8a). The average density ρ is 820-2700 kg/m^3 with 90% confidence, as in the large sphere case. However, since less buoyancy is required for smaller spheres, the density contrast $\Delta\rho$ is permitted to take on lower values (320-2900 kg/m^3 with 90% confidence) as compared to the large sphere case.

For both small and large spheres, the conduit radius R is positively correlated with the magma viscosity μ as it is the parameter combination τ_{vis} that is well constrained. The lower bound for μ in the prior leads to a lower bound for R (~3 m). This is because when R is too narrow, the oscillation becomes overdamped and cannot match the observed quality factor. However, the data has no sensitivity to the upper bound of R.

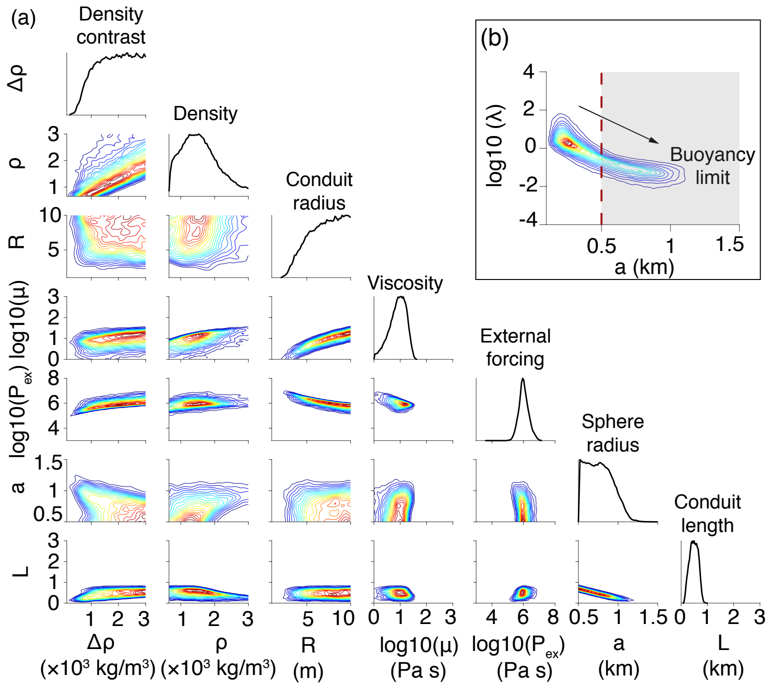

Figure 8. Event 4. (a) Correlation plots of model parameters in the conduit in the large sphere limit ($a >$ 0.5 km). (b) Correlation plots between sphere radius a and stiffness ratio λ, highlighting the region with $a >$ 0.5 km.

5.2 Conduit-crack model

For the conduit-crack model, two possible crack solutions are found for each event as revealed by the bimodal distributions of centroid depth (Z_c), crack length (D), and strike (ϕ) shown in Figure 10. One solution is shallower (centered about 0.8-1 km) but longer (crack length of about 2-3 km) with strike around 250-270° from north (approximately east-west trending). The other solution is deeper (centered about 1.5-2 km) but

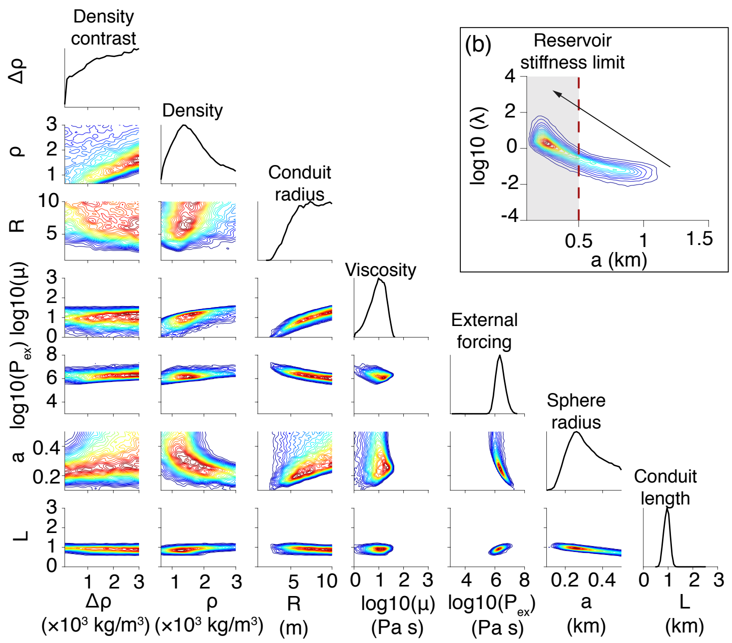

Figure 9. Event 4. (a) Correlation plots of model parameters in the conduit in the small sphere limit ($a <$ 0.5 km). (b) Correlation plots between sphere radius a and stiffness ratio λ, highlighting the region with $a <$ 0.5 km.

much shorter (crack length of about 0.1-0.4 km) with a strike around 280-320° from north. Both cracks have dips less than 40° and the cracks inferred for events 1 and 2 tend to have lower dips (with 95% percentile value less than 30.2°). The east and north locations of the centroid are also reasonably constrained, although about 100-200 m further east from the sphere centroid.

As for the sphere case, we focus on event 4 with results for other events provided in the Supporting Information. Similar to the large sphere, the large crack (D > 1 km) solution corresponds to the the buoyancy limit ($\lambda \ll 1$) with similar storativity (C_t > 0.03 m^3/Pa), as shown in Figure 11. This is anticipated because a crack with length D has a storativity similar to a sphere with $a \sim D/2$ (see Part I). The stiffness ratio λ becomes more comparable to unity or even much larger than unity for smaller crack sizes, as then the reservoir stiffness provides a larger contribution to the restoring force. Both small and large cracks can explain the data similarly well. Similar to a small sphere (a < 0.5 km), a crack with D < 1 km seems incompatible with the range of reservoir storativity inferred from the DI events [*Anderson et al.*, 2015].

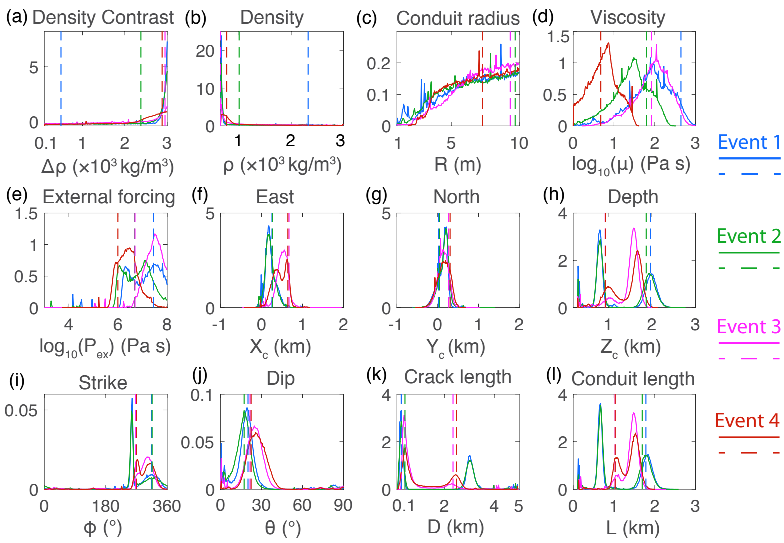

Figure 10. Posterior distributions (solid lines) of model parameters of the conduit-crack model for 4 VLP events with 4 million samples. The conduit length L is calculated from the PDFs of the crack centroid location while all other parameters are directly estimated in the MCMC inversion. The vertical dashed lines indicate the MLE.

The two parameter combinations, T_0 and τ_{vis}, are also well constrained with ranges similar to the conduit-sphere model (Figure 5). The distributions of predicted period and quality factor from the posterior samples are centered around the observed value, with the MLEs matching the observed values. The order of magnitude of viscosity μ and external forcing P_{ex} are reasonably constrained, similar to the conduit-sphere model. For example, the 90% credible interval of viscosity μ for the conduit-crack model is [1.4, 20.9] Pa s for event 4, comparable to [2.1, 22.9] Pa s for the conduit-sphere model. And as before, a lower bound is obtained for the conduit radius (~3 m) but the upper bound is not constrained.

In both the large and small crack solutions (Figures 12 and 13), parameters trade-off in a similar ways as in the conduit-sphere model except that here the crack length D replaces the sphere radius a in characterizing the reservoir stiffness. However, there is a key difference in our assumed conduit-reservoir geometry. Because we assume that the conduit connects to the crack centroid, the conduit length is entirely determined by the crack centroid location and is not affected by the crack size D. (Contrast this to the conduit connecting to the upper edge of the sphere, which mandates an additional constraint between

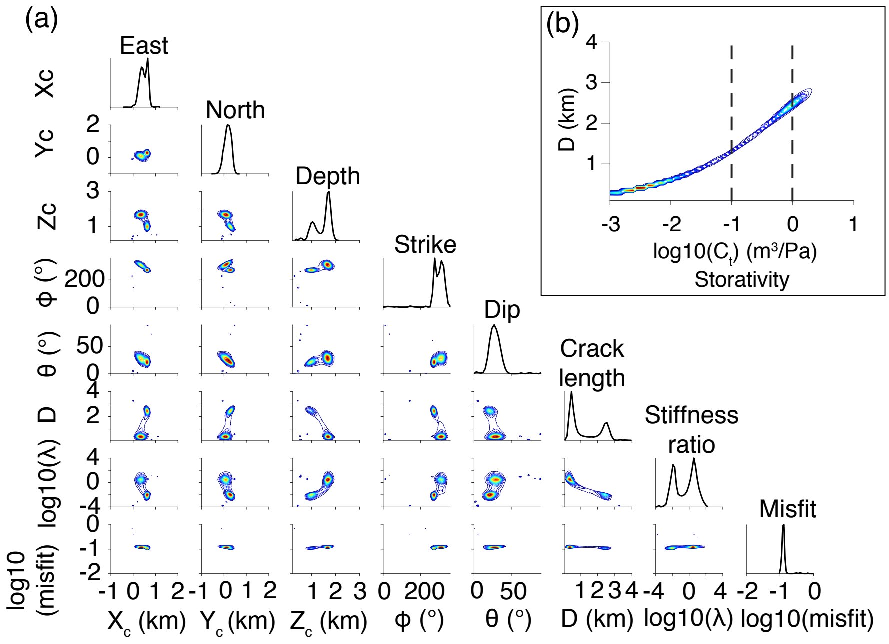

Figure 11. Event 4. Correlation plots of model parameters for the crack, stiffness ratio (λ), and misfit. Similar the large sphere case, the large crack (D > 1 km) solution corresponds the buoyancy limit ($\lambda \ll 1$). (b) Correlation plots between reservoir storativity (C_t) and crack length D. Two dashed lines mark the range 0.1-1 m^3/Pa.

L and a in the sphere model that is not present between L and D in the crack model.) As a result, the estimated conduit length L in the conduit-crack model is generally longer than that in the conduit-sphere model. For event 4, L in the conduit-crack model is 0.93-1.45 km and 1.35-1.71 km for the large and small crack solutions, respectively. At the large crack limit, a much longer conduit in the conduit-crack model thus requires a much higher $\Delta\rho/\rho$ ratio to match the observed oscillation period, resulting in extremely low magma density ρ (650-900 kg/m^3) and high density contrast $\Delta\rho$ (2300-2900 kg/m^3), as shown in Figure 12. To achieve such low average density and high density contrast, magma density must remain close to the lower bound over most of the conduit and then sharply increase to the upper bound near the reservoir, which seems unrealistic. In contrast, the large sphere solution offers a much more reasonable range for both density and density contrast because a large sphere requires a much shorter conduit.

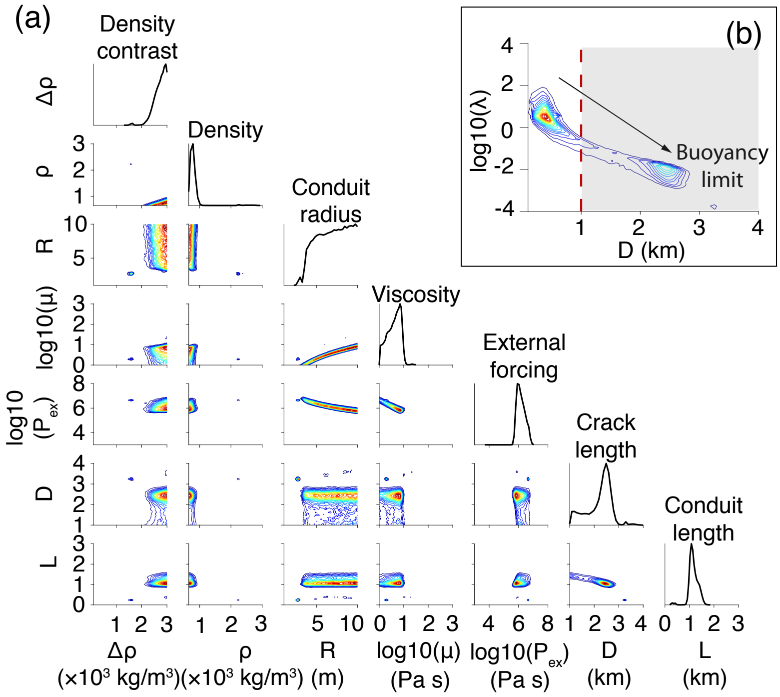

Figure 12. Event 4. (a) Correlation plots of model parameters in the conduit in the large crack limit ($D >$ 1 km). (b) Correlation plots between crack length D and stiffness ratio λ, highlighting the region with $D > 1$ km.

5.3 Model comparison

Since both small sphere and small crack solutions are less appealing due to the small storativities, we compute the BICs using the MLEs of large sphere ($a > 0.5$ km) and large crack ($D > 1$ km) solutions. Based solely on BIC reduction (Table 2), the data seem to favor a conduit-sphere model for events 1 and 2 in 2008 but a conduit-crack model for events 3 and 4 in 2012 and 2013, respectively. However, no notable dike or sill intrusions have been reported around the Kīlauea summit region during the time between events 2 and 3. Thus, the explanation of an originally spherical reservoir evolving into a crack-shaped reservoir over the course of 3 years lacks independent constraints.

Misfits are dominated by those from fitting the surface displacements while the periods and quality factors are well matched by both models. Despite having two fewer free parameters than a crack reservoir, the spherical reservoir fits the surface displacements better than a single crack for events 1 and 2. For events 3 and 4, the computed misfits by the MLEs are slightly lower for a crack compared to a sphere. However, both models ex-

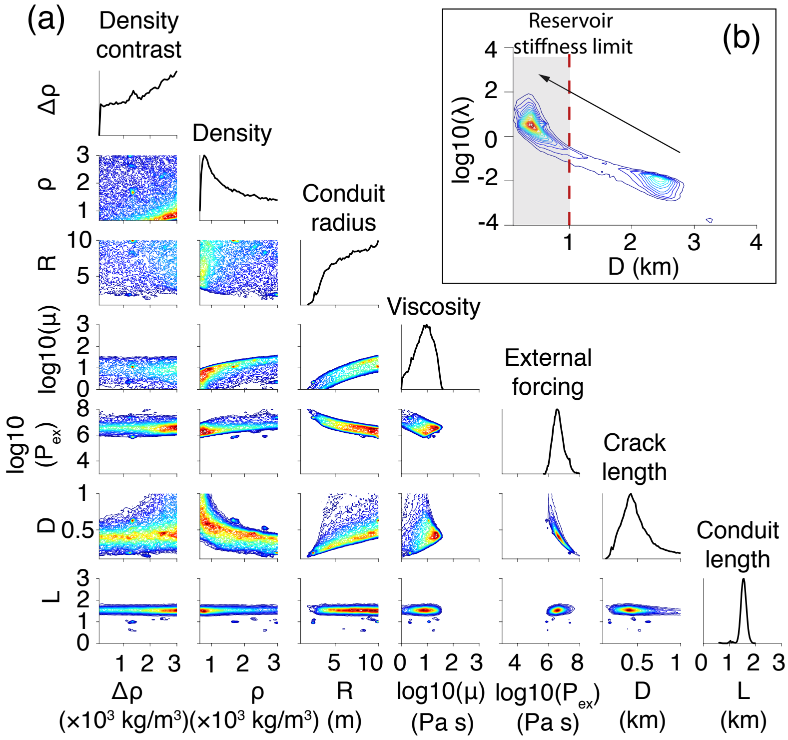

Figure 13. Event 4. (a) Correlation plots of model parameters in the conduit in the small crack limit ($D <$ 1 km). (b) Correlation plots between crack length D and stiffness ratio λ, highlighting the region with $D < 1$ km.

plain the surface displacement pattern quite well, as shown in Figure 14 for event 4 (see Supporting Information for other events). Due to the way we define the standard deviation of the displacements, the crack might be able to better fit the displacements for these large amplitude channels than the sphere but visually the overall fits of both models are reasonably close. Therefore, we conclude that the fitting powers of both models (crack and sphere) to the VLP seismic data are not appreciably different.

6 Discussion

6.1 Kīlauea summit shallow reservoir

As mentioned in the previous section, both a sphere and crack can explain the VLP seismic data at Kīlauea. Our inversions suggest a stable sphere centroid consistent with the shallow Halemaʻumaʻu reservoir inferred geodetically from long timescale DI events by *Anderson et al.* [2015] and generally 0.2-0.5 km deeper than the centroids of the bestfitting point moment tensor (at ∼1 km) found in VLP seismic inversions by *Chouet et al.* [2010] and *Chouet and Dawson* [2013]. Both a large and small sphere can explain the VLP seismic data. However, for the reservoir storativity to be compatible with previous estimates from the DI events [*Anderson et al.*, 2015] as suggested by Liang and Dunham (2019), we reject the small sphere solution (radius less than 0.5 km).

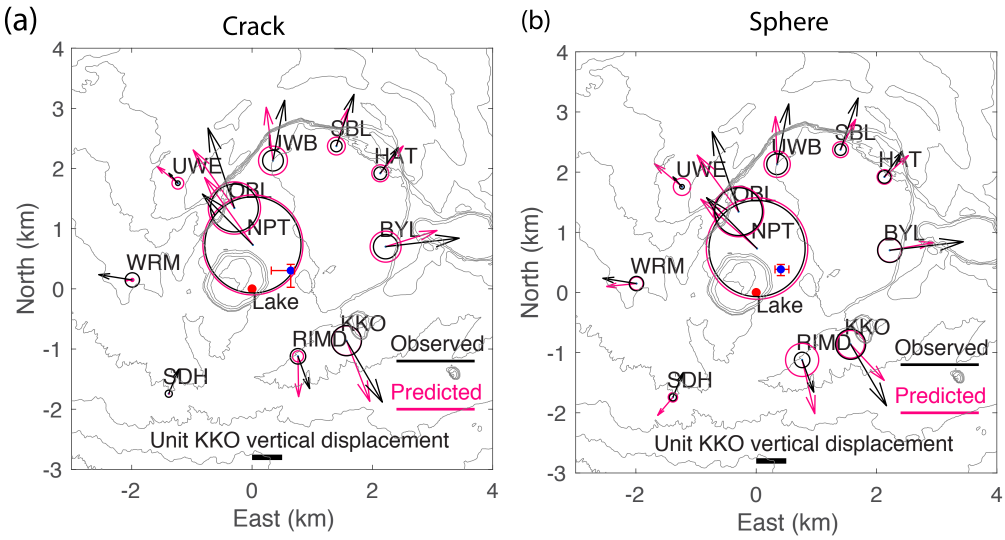

Figure 14. Predicted displacements from the MLE of large crack (D > 1 km) model (a) and large sphere (a > 0.5 km) model (b) for event 4. The diameters of circles indicate the vertical uplifts and arrows indicate horizontal displacements. The thick black horizontal bar marks the scale for KKO vertical displacement. The blue dot marks the horizontal location of the reservoir centroid with red error bars indicating the extent of 90% credible interval. Plots for events 1, 2, and 3 are given in the Supporting Information.

Our inversion also reveals two possible single sill-like solutions: one is larger and shallower and the other is smaller and deeper. By a similar logic with the small sphere solution, we reject the small/deep crack solution due to the inconsistency with independent estimates of reservoir storativity. The larger crack solution (0.8-1 km deep, 2-3 km long, and trending approximately east-westward) seems compatible with the east-west trending dike in the dual system obtain by *Chouet et al.* [2010] and *Chouet and Dawson* [2013] at similar depth. However, our inversion obtains a dip less than 40° as opposed to a sub-vertical dike. The storativity of the large crack solution is similar to that of the large sphere solution. However, the assumption that the conduit connects to the crack centroid results in a much longer conduit for the large crack solution than for the large sphere solution. The long conduit puts highly restrictive constraints on the magma density (close to the lower bound of ~650 kg/m^3) and density contrast (close to ~3000 kg/m^3), a combination that seems unrealistic.

We thus favor a spherical reservoir with radius of 0.8-1.2 km centered around 1.2-1.5 km depth, which is consistent with the previous estimates of reservoir storativity from the DI events and also explains the VLP seismic data with reasonable ranges of magma density and density contrast. The large reservoir size puts the VLP oscillation in the buoyancy-dominated limit where the contribution of reservoir stiffness to the overall restoring force is negligible. Stratification of magma within the conduit is therefore required to provide the necessary buoyancy to create VLP oscillations.

Note that rejecting a single crack connected by a conduit at the crack centroid does not necessarily rule out the dual-dike geometry proposed by *Chouet et al.* [2010] and *Chouet and Dawson* [2013]. Since subvertical dikes are more effective at reaching shallow depths, this dual-dike geometry may also explain the VLP periods with a shallow and short conduit similar to that in the conduit-sphere model. However, contrary to *Chouet and Dawson* [2013] who assume reservoir stiffness to be the primary restoring force, we find buoyancy is more likely to dominate at large crack size (~2.9 km).

In the buoyancy-dominated limit, T_0, a good approximation to T, is well described by (13). Assuming $\sin\beta \approx 1$, we obtain an estimate of conduit length $L \approx (T_0/2\pi)^2\Delta\rho g/\rho$. Assuming $\Delta\rho$ ~2000 kg/m^2 and ρ ~2500 kg/m^2, the range of T_0 (22-40 s) constrains L to be 100-320 m. Thus unless there is evidence for an even higher value of $\Delta\rho/\rho$, a short conduit is necessary for the buoyancy limit to be a viable solution, regardless of reservoir shape (as long as the reservoir size is large enough). To obtain $\Delta\rho$ ~2000 kg/m^2 over a conduit length of a few hundred meters, the density of the lava lake would need to be very low (600-800 kg/m^3) and magma density must increase rapidly within the conduit if we assume the magma density at the bottom of the conduit is near 2600-2800 kg/m^3. A low magma density in the lava lake is consistent with estimates from gravity measurements: 100-200 kg/m^3 at the lava lake surface [*Poland and Carbone*, 2018] and 650-1250 kg/m^3 inside the lava lake [*Carbone et al.*, 2013].

To further improve constraints on the reservoir geometry, additional data should be incorporated. Higher modes in the seismic data [e.g., *Chouet and Dawson*, 2011; *Dawson and Chouet*, 2014] may provide evidence for resonance of crack waves [e.g., *Chouet*, 1986; *Ferrazzini and Aki*, 1987; *Lipovsky and Dunham*, 2015], which are sensitive to crack geometry. Infrasound data [e.g., *Fee et al.*, 2010], together with webcam imagery and high resolution lava lake height [e.g., *Patrick et al.*, 2015], could help to provide better constraints on the impact force generated by impulsive excitations, such as rockfalls and bubble bursts. Future modeling of the detailed excitation process in the lava lake is also necessary to relate the processes on the lava lake surface to the forcing applied to the underlying conduit-reservoir system, thus helping to discriminate different reservoir models.

6.2 What can be constrained from VLP seismic data?

Two parameter combinations T_0 and τ_{vis} are well constrained from the observed period T and quality factor Q. These explain the trade-offs among individual parameters, such that between magma viscosity and conduit radius and that between density and density contrast. Fluctuations in T and Q over daily to yearly time scales [*Dawson and Chouet*, 2014] thus reflect fluctuations of T_0 and τ_{vis} in the magma plumbing system.

In the buoyancy-dominated limit, changes in T_0, as shown in (13), reflect changes in average magma density ρ or density contrast $\Delta\rho$ in the conduit assuming that the conduit length L and dip β remain unchanged. According to *Dawson and Chouet* [2014], T generally evolves slowly over time scales of months (except during rapid lake drainage events) while fluctuations in Q can occur over much smaller time scales of hours or even minutes. Rapid fluctuations of Q, with R and T relatively unchanged (implying no changes to ρ or $\Delta\rho$), therefore indicate a rapid change in viscosity according to (8). These observations therefore provide evidence for the highly dynamic nature of properties such as volatile content and/or magma flow regimes within the shallow magma plumbing system. Large variations in viscosity could have effects on the conduit flow state that may be visible at the lava lake surface as changes in circulation pattern, spattering, or gas pistoning [*Patrick et al.*, 2016].

From our inversions, the order of magnitude of viscosity is reasonably constrained despite the trade-offs with other parameters, and differs across events. Events with large Q put tighter constraints on viscosity. In particular, the viscosity estimated for event 4 (T = 39.2 s and Q = 25.5) is 2-23 Pa s is lower than the range (30-400 Pa s) for basaltic melt inclusions collected by *Edmonds et al.* [2013] but still within the wider range of basaltic melt at Kīlauea reported by *Shaw et al.* [1968]. Both a hotter temperature or a higher volatile content can decrease melt viscosity [*Shaw et al.*, 1968]. At high strain rates, elongated bubbles and bubble coalitions can also substantially decrease the bulk viscosity [e.g., *Manga et al.*, 1998; *Llewellin and Manga*, 2005; *Mader et al.*, 2013].

One possible way to reduce the degree of nonuniqueness is to recognize that magma density, density contrast, and viscosity are related and strongly dependent on the pressure, temperature, and volatile content [e.g., *Mysen*, 1977; *Persikov et al.*, 1990; *Newman and Lowenstern*, 2002; *Burgisser et al.*, 2015; *Wallace et al.*, 2015]. A well constrained equation of state (e.g., solubility model) and flow model can help define the depth dependent properties of the background state. In this study, we neglected some possibly important processes, such as nonequilibrium bubble growth and resorption [*Karlstrom and Dunham*, 2016], a more complex background state involving background flow and relative flow between phases [*Huppert and Hallworth*, 2007; *Fowler and Robinson*, 2018; *Suckale et al.*, 2018], depth-dependent viscosity, and etc. We also neglected complex geometries, such as depth-dependent conduit radius and the possibility of multiple reservoirs.

7 Conclusion

Our inversions can fit the seismic data with a consistent spherical source about 1.2-1.5 km beneath the northeast edge of Halema‘uma‘u crater, consistent with the source region of geodetically observed deflation-inflation events, although both a large and a small sphere can explain the seismic data. Our inversions can also fit the seismic data similarly well with two possible crack configurations, which are similar in the east, north positions, and dips but different in depths, lengths, and strikes.

Considering the reasonable range of reservoir storativity, magma density, and density contrast, we favor the conduit-sphere model with a sphere radius of 0.8-1.2 km and thus a short conduit of less than a few hundred meters long, which then requires buoyancy to be the dominant restoring force. In the buoyancy-dominated limit, changes in T and Q directly reflect changes of magma density, density contrast, and magma viscosity if the geometry of the plumbing system remained unchanged. Future studies could utilize VLP catalogs of T and Q to study evolution of these magma properties during the decade or so of VLP activity at Kīlauea.

In addition, future studies should also combine observations of the conduit-reservoir mode studied here with analysis of higher resonant modes of the system. This requires modeling the fluid dynamics in the lava lake so that the entire plumbing system (lava lake, conduit, and reservoir) can be treated in a fully coupled manner. More rigorous modeling of the lava lake will also provide insight into how different reaction forces induced by rockfalls and bubble bursts are transformed into pressure excitation at the top of the conduit, which in this study is treated as a free parameter with minimal prior knowledge. In addition, independent observations such as gravity measurements, gas measurements, volcano-tectonic seismicity locations, and camera images of lake convection and rockfall sizes could place narrower bounds on the prior distributions of some model parameters.

Acknowledgments

This work was supported by the National Science Foundation (EAR-1624431). We acknowledge the staff and scientists of Hawaiian Volcano Observatory for maintaining and operating the broadband seismic network and webcam imagery at Kīlauea summit. We especially thank Phillip Dawson for sharing the VLP catalog and insightful discussions on the Kīlauea plumbing system. We are grateful to Paul Segall for help on geodetic inversions. The comments from two anonymous reviewers have significantly improved the quality of the manuscript. The waveform data of the two 2008 VLP events can be downloaded from `https://github.com/chaovite/VLP_waveform_data_2008`. Seismic waveform data after mid-2011 can be downloaded from the IRIS Data Management Center. GWMCMC software is available at `https://github.com/grinsted/gwmcmc`. The implementation of the oscillation model is available at `https://github.com/chaovite/conduit_reservoir_oscillator`.

A: Evidence for neglecting acoustic resonance in the conduit

One may be tempted to use resonances of slow acoustic waves in the conduit to explain the ~30 s VLP oscillations at Kīlauea. However, the observations of the timing of a rock fall event and the onset of VLP oscillation shown in Figure A.1 refute this hypothesis. The logic is as follows. Since it takes time for the acoustic wave to propagate from the surface to VLP deformation centroids, a time lag must exist between the timing of the rockfall impact and the onset of the VLP deformation. If conduit acoustic resonance were to explain the ~30 s oscillation period, this time lag must be at least a quarter to half of the period (7-15 s) depending on the boundary conditions at two ends of the conduit. However, from Figure A.1, we observe that the onset of the VLP starts almost immediately (less than 1 s) after the rock fall impact. In Figure A.1, the time delay caused by the propagation of seismic waves from the VLP source centroid to the NPT station is neglected. If this time delay is accounted for, the time difference between the rockfall impact and the VLP onset would be even shorter. The alignment between the unfiltered waveform and the waveform of the VLP band shown in Figure A.1A indicates minimal phase shift induced by the band-pass filter. Given the VLP source centroid depth of ~1 km, the acoustic wave speed in the magma is thus at least 1000 m/s. If the acoustic wave speed is so high, then the predicted conduit resonance frequencies are vastly higher than the VLP frequency given a conduit length of 1-2 km. Conduit acoustic resonances [e.g., *Garces*, 2000; *Karlstrom and Dunham*, 2016] may explain VLP oscillations in other volcanic settings. However, we reject this candidate for the ~30 s VLP oscillations at Kīlauea.

B: Data processing

In this section, we present the detailed data processing steps to extract features necessary for the inversions. The VLP period T is calculated by

$$T = \frac{1}{f_r} \tag{B.1}$$

where f_r is the frequency of the dominant spectral peak. The quality factor Q is extracted from the spectral amplitude of the seismograms by

$$Q = \frac{f_r}{\Delta f} \tag{B.2}$$

where Δf is the width, in frequency units, of the spectral peak at the level of $1/\sqrt{2}$ of the maximum amplitude [*Green*, 1955].

We then extract the spectral value of the displacement waveform $\hat{u}_i$ of each channel (with i as the channel index) at VLP resonant frequency. The total number of channels N_c is equal to $3N_s$, where N_s is the number of stations and the number of components is 3 (east, north, and vertical up). The $\hat{u}_i$ are complemented by the extracted period T and quality factor Q, which altogether are sufficient to characterize the VLP mode.

As a spectral value, $\hat{u}_i$ is a complex number:

$$\hat{u}_i = a_i e^{i\Phi_i}, \tag{B.3}$$

where a_i is the amplitude and Φ_i is the phase. After removing the phase of a reference channel (index 0, the Z component of NPT or NPB) from $U\hat{u}_i$, we have the corrected spectral value of displacement

$$\hat{u}_i' = \frac{\hat{u}_i}{e^{i\Phi_0}} = a_i e^{i(\Phi_i - \Phi_0)} = \hat{u}_i^R + iI_i, \tag{B.4}$$

where Φ_0 is phase of the reference channel, $\hat{u}_i^R$ is the real part of $\hat{u}_i'$, and I_i is the imaginary part of $\hat{u}_i'$. Non-zero I_i/a_i indicate the presence of phase shifts due to seismic wave propagation through different source-station distances and noise in the data. To evaluate the data quality, we compute the noise spectrum using a window of 500 s prior to the start times of the selected VLP events and extract the spectral value of the noise n_i at resonant frequency f_r. We then define the signal-to-noise ratio (SNR) of each channel as

$$SNR_i = \frac{\text{abs}(\hat{u}_i)}{\text{abs}(n_i)}. \tag{B.5}$$

Figure B.1 shows the SNR_i and I_i/a_i of each channel for the 4 VLP events analyzed. For all the 4 events, I_i/a_i of most channels are within the bound of -0.1 to 0.1. The one or two channels exceeding the bound either are due to small SNR or have small amplitudes a_i (~10 fold smaller) compared to that of the reference channel a_0. The SNR of most channels are also above 10 with one or two exceptions, which are associated with small amplitudes a_i/a_0. Thus, in this work, we assume quasi-static elasticity for the solid Earth's response and only model the real parts $\hat{u}_i^R$. Non-zero I_i/a_i and low SNR_i are lumped into the noise model for MCMC inversion. In particular, the factor of 10, reflecting both the bounds of I_i/a_i and SNR are used to set the data standard deviation.

C: Prior distribution and data likelihood function

We assume relatively broad priors with a uniform distribution and large bounds for all model parameters (Table 1). We require the depth of the reservoir top Z_t to be greater than the depth of the lava lake bottom Z_0. Since the bottom of lava lake is about 0.2 km below the Halema'uma'u Crater floor [*Fee et al.*, 2010; *Patrick et al.*, 2013], we set $Z_0 = 0.2$ km, which sets the lower bound for Z_t. Since the centroids of VLPs are consistently located at depths of ∼1 km, we bound Z_t to be less than 3 km. The East and North of the reservoir centroid must be bounded within the extent of Halema'uma'u Crater as suggested by the surface deformation pattern shown in Figure 4. Since *Chouet and Dawson* [2011] estimate the crack length as long as 2.9 km, we assume crack length D to vary from 0.1 to 5 km. We also assume the radius of the sphere is bounded from 0.1 to 2 km.

Putting bounds on the parameters in the conduit is more challenging. Even though the conduit radius is ∼5 m at the bottom of the lava lake as observed by forward looking infrared (FLIR) imagery in late 2008 to early 2009 [*Fee et al.*, 2010], direct observation of conduit radius at depth is not possible. We assume conduit radius R is bounded between 1 and 10 m. The density of shallow magma can have large variation due to bubble exsolution [*Carey et al.*, 2012; *Edmonds et al.*, 2013; *Orr et al.*, 2013]. At Kīlauea Volcano, the ejected pyroclasts from the 12 October 2008 eruption triggered by rockfalls exhibit a bulk density of 310-1000 kg/m^3 (a volume fraction of 89-62%) [*Carey et al.*, 2012]. The density of volatile-free melt is thus ∼2900 kg/m^3, comparable to ∼2700 kg/m^3 estimated by *Edmonds et al.* [2013] from melt inclusions. *Poland and Carbone* [2018] found, from gravity data, very low density (100-200 kg/m^3) foam near the surface of the lava lake during gas pistons. However, the gas pistons only involve fluctuation of the top ∼20 m of the lava lake and may not be representative of the deeper lake. Gravity measurements during 120 m of lava lake retreat in 2011 suggest the lava lake is gas-rich and has a magma density of 950 ± 300 kg/m^3 [*Carbone et al.*, 2013]. We expect the magma density in the conduit to be higher than that in the lava lake, so we bound average magma density in the conduit ρ between 650 to 3000 kg/m^3. We expect the magma density in the reservoir to be higher than that at the top of the conduit. However, we do not have enough information to put narrower bounds on the density contrast $\Delta\rho$ between the bottom and the top of the conduit. Thus, we assume a wide bound for $\Delta\rho$, 100-3000 kg/m^3. We assume that the viscosity μ is bounded between 1 and 1000 Pa s, appropriate for basaltic magma at Kīlauea [*Shaw et al.*, 1968; *Carey et al.*, 2012].

An accurate estimate of P_{ex} requires detailed modeling of complex physical process in the lava lake during rockfall or degassing, which is beyond the scope of this study. We thus decide to choose a large bound for this parameter. Although the excitation is not limited to rockfall, we use the impact generated by rockfalls as a reference. *Carey et al.* [2012] concludes rockfalls onto the magma surface can generate impact pressure on the order of a few to tens of MPa immediately below the impact site. Although this overpressure might have decayed when the pressure wave reaches the top of the conduit at the lava lake floor, we conservatively choose 10^8 Pa s as the upper bound for P_{ex}, which is equivalent to a pressure pulse with amplitude of 100 MPa and duration of 1 s. The lower bound for P_{ex} is set to 10^3 Pa s which corresponds to a pressure pulse with amplitude of 1 kPa and duration of 1 s. Since P_{ex} can vary over many orders of magnitude, we use the logarithm of P_{ex} as the model parameter. The same bounds are used for all four events.

We assume that the data likelihood function follows independent Gaussian distributions

$$P(\mathbf{d}|\mathbf{m}) \propto \exp\left(-\frac{(T-T_{pred})^2}{2\sigma_T^2} - \frac{(Q-Q_{pred})^2}{2\sigma_Q^2} - \sum_i^{N_c} \frac{(\hat{u}_i^R - \hat{u}_{i,pred}^R)^2}{2\sigma_{u_i}^2}\right), \tag{C.1}$$

where T_{pred}, Q_{pred}, and $\hat{u}_{i,pred}^R$ are the predicted period, quality factor, and displacement, and σ_T, σ_Q, and σ_{u_i} are the standard deviation of period, quality factor and displacement of each channel. The measurements of period and quality factor are quite accurate and we assume $\sigma_T = 1$ s and $\sigma_Q = 1$. According to Figure B.1, even though the signal-to-noise ratios for most channels are higher than 10, we observe up to 10% imaginary parts in $\hat{u}_i'$ and also notice that channels with smaller amplitudes tend to have smaller SNR and larger I_i/a_i. Therefore, we assume σ_{u_i} to be 10% of a_0 (the amplitude of vertical displacement of station NPT or NPB). Since a_0 is the maximum of all a_i, this choice for σ_{u_i} assigns more importance to channels with larger displacement amplitudes. To discard the horizontal displacements of SDH for events 3 and 4 (unexplainable opposite polarity), we simply set the its standard deviation to a large value ($1000a_0$).

To aid the evaluation of MLE, we also define a misfit function similar to *Chouet and Dawson* [2013]:

$$\text{misfit} = \text{misfit}_{TQ} + \text{misfit}_u, \tag{C.2}$$

where

$$\text{misfit}_{TQ} = (T-T_{pred})^2/T^2 + (Q-Q_{pred})^2/Q^2, \tag{C.3}$$

$$\text{misfit}_u = \frac{\sum_i^{N_c} (\hat{u}_i^R - \hat{u}_{i,pred}^R)^2}{\sum_i^{N_c} (\hat{u}_i^R)^2}, \tag{C.4}$$

are the misfits due to fitting period and quality factor and the misfit due to fitting the displacements.

References

Almendros, J., B. Chouet, P. Dawson, and T. Bond (2002), Identifying elements of the plumbing system beneath Kilauea Volcano, Hawaii, from the source locations of very-long-period signals, *Geophysical Journal International*, *148*(2), 303–312, doi:10.1046/j.1365-246X.2002.01629.x.

Anderson, K. R., M. P. Poland, J. H. Johnson, and A. Miklius (2015), *Episodic Deflation-Inflation Events at Kīlauea Volcano and Implications for the Shallow Magma System*, chap. 11, pp. 229–250, American Geophysical Union (AGU), doi:10.1002/9781118872079.ch11.

Aster, R., S. Mah, P. Kyle, W. McIntosh, N. Dunbar, J. Johnson, M. Ruiz, and S. McNamara (2003), Very long period oscillations of Mount Erebus Volcano, *Journal of Geophysical Research: Solid Earth*, *108*(B11), doi:10.1029/2002JB002101.

Aster, R., D. Zandomeneghi, S. Mah, S. McNamara, D. Henderson, H. Knox, and K. Jones (2008), Moment tensor inversion of very long period seismic signals from Strombolian eruptions of Erebus Volcano, *Journal of Volcanology and Geothermal Research*, *177*(3), 635–647, doi:10.1016/j.jvolgeores.2008.08.013.

Burgisser, A., M. Alletti, and B. Scaillet (2015), Simulating the behavior of volatiles belonging to the c–o–h–s system in silicate melts under magmatic conditions with the software d-compress, *Computers & Geosciences*, *79*, 1–14, doi:10.1016/j.cageo.2015.03.002.

Carbone, D., M. P. Poland, M. R. Patrick, and T. R. Orr (2013), Continuous gravity measurements reveal a low-density lava lake at Kīlauea volcano, Hawai'i, *Earth and planetary science letters*, *376*, 178–185.

Carey, R. J., M. Manga, W. Degruyter, D. Swanson, B. Houghton, T. Orr, and M. Patrick (2012), Externally triggered renewed bubble nucleation in basaltic magma: The 12 October 2008 eruption at Halema'uma 'u Overlook vent, Kīlauea, Hawai'i, USA, *Journal of Geophysical Research: Solid Earth*, *117*(B11), doi:10.1029/2012JB009496.

Carey, R. J., M. Manga, W. Degruyter, H. Gonnermann, D. Swanson, B. Houghton, T. Orr, and M. Patrick (2013), Convection in a volcanic conduit recorded by bubbles, *Geology*, *41*(4), 395–398, doi:10.1130/G33685.1.

Cervelli, P. F., and A. Miklius (2003), *The Shallow Magmatic System of Kīlauea Volcano*, chap. 9, pp. 149–164, Professional Paper 1676, U.S. Geological Survey, Reston, Virginia.

Chouet, B. (1986), Dynamics of a fluid-driven crack in three dimensions by the finite difference method, *Journal of Geophysical Research: Solid Earth*, *91*(B14), 13,967–13,992, doi:10.1029/JB091iB14p13967.

Chouet, B., and P. Dawson (1997), Observations of very-long-period impulsive signals accompaying summit inflation at Kilauea Volcano, Hawaii, in february 1997, *EOS, Trans. Am. geophys. Un.*, *76*.

Chouet, B., and P. Dawson (2011), Shallow conduit system at Kilauea Volcano, Hawaii, revealed by seismic signals associated with degassing bursts, *Journal of Geophysical Research: Solid Earth*, *116*(B12), doi:10.1029/2011JB008677.

Chouet, B., and P. Dawson (2013), Very long period conduit oscillations induced by rockfalls at Kilauea Volcano, Hawaii, *Journal of Geophysical Research: Solid Earth*, *118*(10), 5352–5371, doi:10.1002/jgrb.50376.

Chouet, B. A., P. B. Dawson, M. R. James, and S. J. Lane (2010), Seismic source mechanism of degassing bursts at Kilauea Volcano, Hawaii: Results from waveform inversion in the 10-50 s band, *Journal of Geophysical Research: Solid Earth*, *115*(B9), doi: 10.1029/2009JB006661.

Crouch, S. L., A. M. Starfield, and F. Rizzo (1983), Boundary element methods in solid mechanics, *Journal of Applied Mechanics*, *50*, 704.

Dawson, P., and B. Chouet (2014), Characterization of very-long-period seismicity accompanying summit activity at Kilauea Volcano, Hawai'i: 2007-2013, *Journal of Volcanology and Geothermal Research*, *278-279*, 59 – 85, doi:https://doi.org/10.1016/j.jvolgeores.2014.04.010.

Dawson, P., B. Chouet, P. Okubo, A. Villaseñor, and H. Benz (1999), Three-dimensional velocity structure of the kilauea caldera, hawaii, *Geophysical Research Letters*, *26*(18), 2805–2808, doi:10.1029/1999GL005379.

Dawson, P., D. Whilldin, and B. Chouet (2004), Application of near real-time radial semblance to locate the shallow magmatic conduit at Kilauea Volcano, Hawaii, *Geophysical Research Letters*, *31*(21), doi:10.1029/2004GL021163.

Dawson, P. B., M. C. Benítez, B. A. Chouet, D. Wilson, and P. G. Okubo (2010), Monitoring very-long-period seismicity at Kilauea Volcano, Hawaii, *Geophysical Research Letters*, *37*(18), doi:10.1029/2010GL044418.

Edmonds, M., I. Sides, D. Swanson, C. Werner, R. Martin, T. Mather, R. Herd, R. Jones, M. Mead, G. Sawyer, et al. (2013), Magma storage, transport and degassing during the

2008–10 summit eruption at kīlauea volcano, hawai âĂŸi, *Geochimica et Cosmochimica Acta*, *123*, 284–301, doi:10.1016/j.gca.2013.05.038.

Fee, D., M. Garcés, M. Patrick, B. Chouet, P. Dawson, and D. Swanson (2010), Infrasonic harmonic tremor and degassing bursts from Halema'uma'u Crater, Kilauea Volcano, Hawai'i, *Journal of Geophysical Research: Solid Earth*, *115*(B11), doi:10.1029/2010JB007642.

Ferrazzini, V., and K. Aki (1987), Slow waves trapped in a fluid-filled infinite crack: Implication for volcanic tremor, *Journal of Geophysical Research: Solid Earth*, *92*(B9), 9215–9223, doi:10.1029/JB092iB09p09215.

Fowler, A., and M. Robinson (2018), Counter-current convection in a volcanic conduit, *Journal of Volcanology and Geothermal Research*, *356*, 141–162, doi:10.1016/j.jvolgeores.2018.03.004.

Garces, M. (2000), Theory of acoustic propagation in a multi-phase stratified liquid flowing within an elastic-walled conduit of varying cross-sectional area, *Journal of volcanology and geothermal research*, *101*(1-2), 1–17, doi:10.1016/S0377-0273(00)00155-4.

Goodman, J., and J. Weare (2010), Ensemble samplers with affine invariance, *Communications in applied mathematics and computational science*, *5*(1), 65–80.

Green, E. I. (1955), The story of q, *American Scientist*, *43*(4), 584–594.

Grinsted, A. (2014), GWMCMC: an implementation of the Goodman & Weare MCMC sampler for matlab, `https://github.com/grinsted/gwmcmc`.

Huppert, H. E., and M. A. Hallworth (2007), Bi-directional flows in constrained systems, *Journal of Fluid Mechanics*, *578*, 95–112, doi:10.1017/S0022112007004661.

HVO (2016), *Jan. 8 rockfall and lava lake explosion at Halema'uma'u Crater*, https://www.youtube.com/watch?v=3YRts3kG8Nk, accessed: September 10, 2018.

Karlstrom, L., and E. M. Dunham (2016), Excitation and resonance of acoustic-gravity waves in a column of stratified, bubbly magma, *Journal of Fluid Mechanics*, *797*, 431–470, doi:10.1017/jfm.2016.257.

Kass, R. E., and A. E. Raftery (1995), Bayes factors, *Journal of the american statistical association*, *90*(430), 773–795.

Liang, C., L. Karlstrom, and E. M. Dunham (2019), Magma oscillations in a conduit-reservoir system, applications to very long period (VLP) seismicity at basaltic volcanoes–Part I: theory, manuscript submitted for publication.

Lipovsky, B. P., and E. M. Dunham (2015), Vibrational modes of hydraulic fractures: Inference of fracture geometry from resonant frequencies and attenuation, *Journal of Geophysical Research: Solid Earth*, *120*(2), 1080–1107, doi:10.1002/2014JB011286.

Llewellin, E., and M. Manga (2005), Bubble suspension rheology and implications for conduit flow, *Journal of Volcanology and Geothermal Research*, *143*(1-3), 205–217, doi: 10.1016/j.jvolgeores.2004.09.018.

Mader, H., E. Llewellin, and S. Mueller (2013), The rheology of two-phase magmas: A review and analysis, *Journal of Volcanology and Geothermal Research*, *257*, 135–158.

Maeda, Y., M. Takeo, and T. Ohminato (2011), A waveform inversion including tilt: method and simple tests, *Geophysical Journal International*, *184*(2), 907–918, doi: 10.1111/j.1365-246X.2010.04892.x.

Mah, S. (2003), Discrimination of Strombolian eruption types using very long period (VLP) seismic signals and video observations at Mount Erebus, Antarctica, *MS Independent Study, New Mexico Institute of Mining and Technology*.

Manga, M., J. Castro, K. V. Cashman, and M. Loewenberg (1998), Rheology of bubble-bearing magmas, *Journal of Volcanology and Geothermal Research*, *87*(1-4), 15–28, doi: 10.1016/S0377-0273(98)00091-2.

McTigue, D. (1987), Elastic stress and deformation near a finite spherical magma body: resolution of the point source paradox, *Journal of Geophysical Research: Solid Earth*, *92*(B12), 12,931–12,940, doi:10.1029/JB092iB12p12931.

Mogi, K. (1958), Relations between the eruptions of various volcanoes and the deformations of the ground surfaces around them, *Bull. Earthquake Res Inst. Univ. Tokyo*, *36*, 99–134.

Mosegaard, K., and A. Tarantola (1995), Monte carlo sampling of solutions to inverse problems, *Journal of Geophysical Research: Solid Earth*, *100*(B7), 12,431–12,447, doi: 10.1029/94JB03097.

Mysen, B. O. (1977), The solubility of h2o and co2 under predicted magma genesis conditions and some petrological and geophysical implications, *Reviews of Geophysics*, *15*(3), 351–361, doi:10.1029/RG015i003p00351.

Newman, S., and J. B. Lowenstern (2002), Volatilecalc: a silicate melt–h2o–co2 solution model written in visual basic for excel, *Computers & Geosciences*, *28*(5), 597–604, doi: 10.1016/S0098-3004(01)00081-4.

Ohminato, T., B. A. Chouet, P. Dawson, and S. Kedar (1998), Waveform inversion of very long period impulsive signals associated with magmatic injection beneath Kilauea Volcano, Hawaii, *Journal of Geophysical Research: Solid Earth*, *103*(B10), 23,839–23,862, doi:10.1029/98JB01122.

Okada, Y. (1985), Surface deformation due to shear and tensile faults in a half-space, *Bulletin of the seismological society of America*, *75*(4), 1135–1154.

Okada, Y. (1992), Internal deformation due to shear and tensile faults in a half-space, *Bulletin of the Seismological Society of America*, *82*(2), 1018–1040.

Orr, T. R., W. A. Thelen, M. R. Patrick, D. A. Swanson, and D. C. Wilson (2013), Explosive eruptions triggered by rockfalls at Kīlauea volcano, Hawai‘i, *Geology*, *41*(2), 207–210, doi:10.1130/G33564.1.

Patrick, M., D. Wilson, D. Fee, T. Orr, and D. Swanson (2011), Shallow degassing events as a trigger for very-long-period seismicity at Kīlauea Volcano, Hawai‘i, *Bulletin of Volcanology*, *73*(9), 1179–1186, doi:10.1007/s00445-011-0475-y.

Patrick, M. R., T. R. Orr, A. J. Sutton, T. Elias, and D. A. Swanson (2013), The first five years of Kīlauea's summit eruption in Halema‘uma‘u Crater, 2008–2013: U.s. geological survey fact sheet 2013-3116, 4 p, *Tech. rep.*, US Geological Survey, doi: 10.3133/fs20133116.

Patrick, M. R., K. R. Anderson, M. P. Poland, T. R. Orr, and D. A. Swanson (2015), Lava lake level as a gauge of magma reservoir pressure and eruptive hazard, *Geology*, *43*(9), 831–834, doi:10.1130/G36896.1.

Patrick, M. R., T. Orr, A. Sutton, E. Lev, W. Thelen, and D. Fee (2016), Shallowly driven fluctuations in lava lake outgassing (gas pistoning), kīlauea volcano, *Earth and Planetary Science Letters*, *433*, 326–338, doi:10.1016/j.epsl.2015.10.052.

Persikov, E. S., V. A. Zharikov, and P. G. Bukhtiyarov (1990), The effect of volatiles on the properties of magmatic melts, *European Journal of Mineralogy*, pp. 621–642.

Poland, M. P., and D. Carbone (2018), Continuous gravity and tilt reveal anomalous pressure and density changes associated with gas pistoning within the summit lava lake of kīlauea volcano, hawai‘i, *Geophysical Research Letters*, *45*(5), 2319–2327, doi: 10.1002/2017GL076936.

Rivalta, E., and P. Segall (2008), Magma compressibility and the missing source for some dike intrusions, *Geophysical Research Letters*, *35*(4), doi:10.1029/2007GL032521.

Rowe, C., R. Aster, P. Kyle, R. Dibble, and J. Schlue (2000), Seismic and acoustic observations at Mount Erebus volcano, Ross island, Antarctica, 1994-1998, *Journal of Volcanology and Geothermal Research*, *101*(1-2), 105–128, doi:10.1016/S0377-0273(00)00170-0.

Ryan, M. (1987), The elasticity and contractancy of hawaiian olivine tholeiite, and its role in the stability and structural evolution of sub-caldera magma reservoirs and rift systems. in volcanism in hawaii, *US Geol. Surv. Prof. Pap.*, *1350*, 1395–1447.

Schwarz, G., et al. (1978), Estimating the dimension of a model, *The annals of statistics*, *6*(2), 461–464, doi:10.1214/aos/1176344136.

Segall, P. (2010), *Earthquake and Volcano Deformation*, Princeton University Press.

Shaw, H., T. Wright, D. Peck, and R. Okamura (1968), The viscosity of basaltic magma; an analysis of field measurements in makaopuhi lava lake, hawaii, *American Journal of Science*, *266*(4), 225–264, doi:10.2475/ajs.266.4.225.

Shima, M. (1958), Counter-current convection in a volcanic conduit, *Disaster Prevention Research Institute, Kyoto University, Bulletins*, *22*, 1–6.

Suckale, J., Z. Qin, D. Picchi, T. Keller, and I. Battiato (2018), Bistability of buoyancy-driven exchange flows in vertical tubes, *Journal of Fluid Mechanics*, *850*, 525–550, doi:10.1017/jfm.2018.382.

Wallace, P. J., T. Plank, M. Edmonds, and E. H. Hauri (2015), Chapter 7 - volatiles in magmas, in *The Encyclopedia of Volcanoes (Second Edition)*, edited by H. Sigurdsson, second edition ed., pp. 163 – 183, Academic Press, Amsterdam, doi:https://doi.org/10.1016/B978-0-12-385938-9.00007-9.

Wilson, D., T. Elias, T. Orr, M. Patrick, J. Sutton, and D. Swanson (2008), Small explosion from new vent at Kīlauea's summit, *EOS, Transactions American Geophysical Union*, *89*(22), 203–203, doi:10.1029/2008EO220003.

Table 1. Model parameters and bounds used in the prior

Parameter	Symbol	Bound or value	Unit	Type
Conduit				
Conduit radius	R	[1, 10]	m	model
Magma density contrast	$\Delta\rho$	[100, 3000]	kg/m^3	model
Average magma density	ρ	[650, 3000]	kg/m^3	model
Magma viscosity	μ	[1, 1000]	Pa s	model
Spectral amplitude of external forcing	P_{ex}	[10^3, 10^8]	Pa s	model
Conduit length	L	-	m	calculated
Conduit dip angle	β	-	radian	calculated
Crack				
Crack length (square crack)	D	[0.1, 5]	km	model
Centroid East	X_c	[-1, 2]	km	model
Centroid North	Y_c	[-1, 2]	km	model
Top edge depth	Z_t	[0.2, 3]	km	model
Strike	ϕ	[0, 359]	°	model
Dip	θ	[0, 90]	°	model
Centroid depth	Z_c	-	km	calculated
Sphere				
Sphere radius	a	[0.1, 2]	km	model
Centroid East	X_c	[-1, 2]	km	model
Centroid North	Y_c	[-1, 2]	km	model
Top depth	Z_t	[0.2, 3]	km	model
Centroid depth	Z_c	-	km	calculated
Constants				
Gravitational acceleration	g	9.8	m^2/s	constant
Solid shear modulus	G	10	GPa	constant
Solid Poisson's ratio	ν_s	0.25	–	constant
Lava lake bottom depth	Z_0	0.2	km	constant
Lava lake East	X_0	0	km	constant
Lava lake North	Y_0	0	km	constant

Note. Unit "–" means non-dimensional. Bound or value "-" means that the bound or value are calculated from other model parameters. Parameters are categorized into three types: "model" (independent parameters), "calculated" (dependent parameters), and "constant" (fixed parameters).

Table 2. Model comparison with BICs.

Event	Model	BIC	misfit_u	misfit_{TQ}
1	large sphere	-284.07	0.056795	0.000209
	large crack	-232.60	0.125542	0.022385
2	large sphere	-292.01	0.037354	0.000167
	large crack	-262.51	0.089517	0.005389
3	large sphere	-180.76	0.131207	0.000491
	large crack	-197.77	0.091491	0.001303
4	large sphere	-226.40	0.151143	0.000075
	large crack	-249.41	0.096008	0.000020

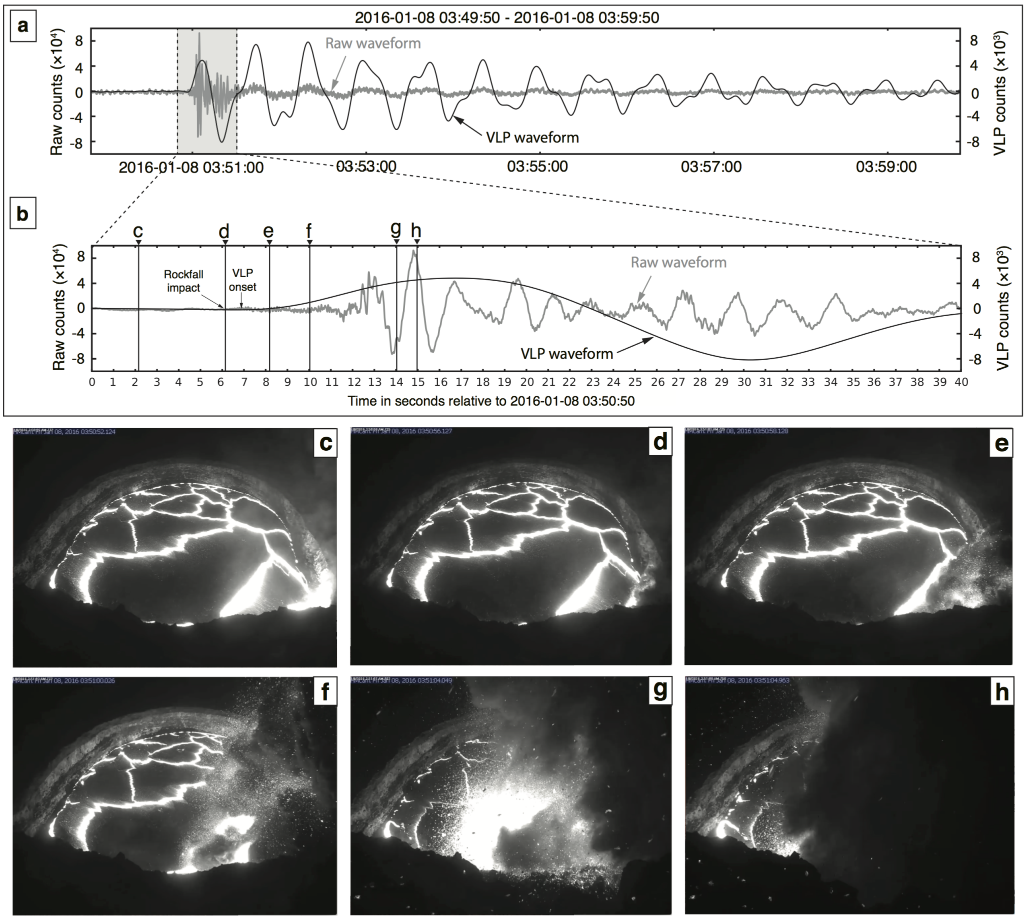

Figure A.1. Comparison between webcam images [*HVO*, 2016] and seismicity for a rock fall event at Kīlauea volcano at 03:50:56 (HST) on 8 January 2016. (a) The vertical velocity seismogram at station NPT in raw counts (gray line) and in the VLP band (dark line, band-passed to 0.002-0.1 Hz) for 10 minutes since 3:49:50 (HST) on 8 January 2016. Note the different scale for raw waveform (left axis) and the waveform in the VLP band (right axis). (b) Vertical velocity seismograms at NPT station in raw counts (gray line) and VLP band (dark line) in a 40 s window marked by the shaded area in (a), enclosing the rockfall impact and initial eruptive activity. The black arrows labeled show the times of rockfall impact the lake surface and the VLP onset. The vertical black lines labeled from c-h correspond to 6 time-stamped webcam images, showing the lake surface prior to rock fall (c), rockfall impacting the lake surface (d), beginning of eruption (e) and subsequent eruptive activities (f, g, h). (c)-(h) Time-stamped webcam images.

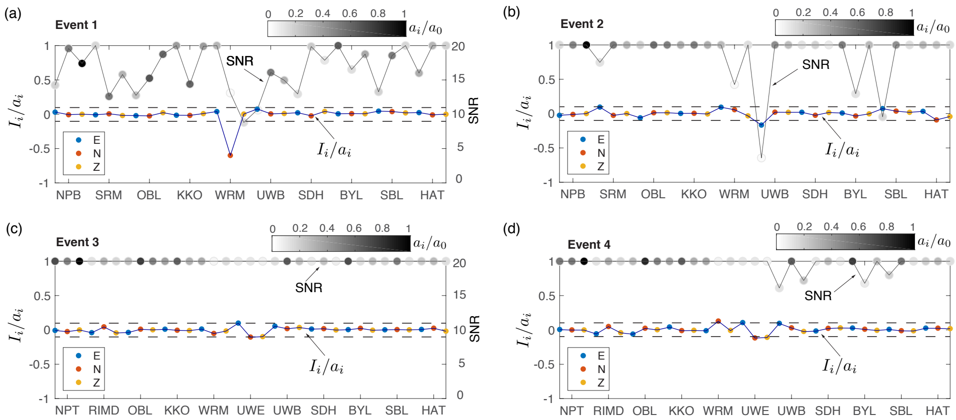

Figure B.1. Imaginery part in spectral value over amplitude I_i/a_i (blue solid line, left axis) and signal-to-noise ratio SNR_i (gray solid line, right axis, capped at 20) of each channel for 4 selected VLP events. The dots on the curve for I_i/a_i are colored by component (E for East, N for North, and Z for vertical up). The black dashed lines indicate the bound of -0.1 to 0.1 for I_i/a_i. The dots on the curve for SNR are colored in gray scale by a_i/a_0. For all the VLP events, most channels have $|I_i/a_i|$ smaller than 0.1 and SNR greater than 10 except for one or two channels, which are associated with small amplitudes a_i compared to that of the reference channel a_0.